RESEARCH ARTICLE

Vascular Endothelial Growth Factor-Recruiting Nanofiber Bandages Promote Multifunctional Skin Regeneration via Improved Angiogenesis and Immunomodulation

Yi Chen[1,2] · Zhengchao Yuan[3] · Weiyan Sun[1,2] · Shafiq Muhammad[3,6,8] · Jun Zhu[4] · Jiafei Chen[1,2] · Hai Tang[1,2] · Ling Hu[5] · Weikang Lin[1,2] · Yanxi Zeng[7] · Long Wang[1,2] · Lei Zhang[1,2] · Yunlang She[1,2] · Hui Zheng[1,2] · Guofang Zhao[9,10] · Dong Xie[1,2] · Xiumei Mo[3] · Chang Chen[1,2]

Abstract

Tissue injury leads to gradients of chemoattractants, which drive multiple processes for tissue repair, including the inflammatory response as well as endogenous cell recruitment. However, a limited time window for the gradients of chemoattractants as well as their poor stability at the injury site may not translate into healthy tissue repair. Consequently, intelligent multifunctional scaffolds with the capability to stabilize injury-induced cytokines and chemokines hold great promise for tissue repair. Vascular endothelial growth factor (VEGF) plays a significant role in wound healing by promoting angiogenesis. The overarching objective of this research was to develop intelligent multifunctional scaffolds with the capability to endogenously recruit VEGF and promote wound healing via angiogenic and immunomodulatory dual functions. Prominin-1-derived peptide (PR1P) was encapsulated into electrospun poly(L-lactide-coglycolide)/gelatin (P/G)-based bandages. The sustained release of PR1P recruited VEGF in situ, thereby stabilizing the protein concentration peak in vivo and affording a reparative microenvironment with an adequate angiogenic ability at the wound site. Meanwhile, PR1P-recruited VEGF-induced macrophage reprogramming towards M2-like phenotypes further conferred immunomodulatory functions to the bandages. These dual functions of proangiogenesis and immunomodulation formed a cascade amplification, which regulated matrix metalloproteinases (MMP-9) as well as inflammatory factors (nuclear factor (NF)-κb, tumor necrosis factor (TNF)-α) in the wound microenvironment via the VEGF/macrophages/microenvironment axis. Consequently, the bandages realized multifunctional regeneration in splinted excisional wounds in rats, with or without diabetes, affording a higher skin appendage neogenesis, sensory function, and collagen remodeling. Conclusively, our approach encompassing in situ recruitment of VEGF at the injury site with the capability to promote immunomodulation-mediated tissue repair affords a promising avenue for scarless wound regeneration, which may also have implications for other tissue engineering disciplines.

Keywords Skin regeneration · Angiogenesis · Immunomodulation · Peptide · Wound bandage · Electrospun nanofiber

Introduction

Complex wounds, including large-scale wounds, diabetic wounds, burns, and chronic nonhealing ulcers caused by diabetes or circulatory disorders, are tedious to heal [1, 2]. Extracellular matrix (ECM) degeneration also leads to disordered angiogenesis, which further delays wound healing, possibly due to the limited diffusion of oxygen and the poor transport of nutrients [3, 4]. In addition, in complex wounds, events such as a high glycemic environment, inflammatory response, or abnormal cellular activation may also dysregulate growth factors (GFs), thus further contributing to imbalanced angiogenesis [5].

Yi Chen, Zhengchao Yuan and Weiyan Sun have contributed equally to this work.

✉ Dong Xie
Kongduxd@163.com

✉ Xiumei Mo
xmm@dhu.edu.cn

✉ Chang Chen
changchenc@tongji.edu.cn

Extended author information available on the last page of the article

Vascular endothelial growth factor (VEGF), a predominant vasculogenic and angiogenic factor in vitro and in vivo, is severely disrupted in complex wounds, thus further restricting wound healing [6, 7]. Many studies have attempted to stabilize the VEGF concentration to promote angiogenesis for wound healing [8–10]. However, owing to its large molecular weight and short half-life [11], VEGF is difficult to synthesize or incorporate into scaffolds. In addition, VEGF can be rapidly degraded or eluted from the injury site, which may further preclude its therapeutic benefits [12–15]. Consequently, different types of approaches, including plasmid-based VEGF gene delivery and micro-/nanocarrier-based VEGF delivery, have been pursued to maintain VEGF gradients to promote angiogenesis for effective tissue repair. Despite potential merits, safety concerns as well as laborious procedures hamper the clinical application of VEGF.

This situation has been partly addressed by designing VEGF-mimetic peptides, such as QK [16], as well as intelligent multifunctional scaffolds to immobilize VEGF in vitro and in vivo. Of notable interest are the studies from Hubbel and colleagues focusing on the fibrin domains to specifically bind VEGF in situ [17]. In addition, glycosaminoglycans (GAGs), such as heparin, have been exploited to electrostatically immobilize heparin-binding GFs, including VEGF, to promote angiogenesis [18]. While these studies have helped enable the controlled release of VEGF as well as angiogenesis for functional tissue repair, extensive ex vivo manipulations limit their clinical applicability from a tissue engineering perspective.

In situ binding of VEGF at the injury site offers a viable approach for inducing tissue repair. While GAG-based materials may electrostatically immobilize heparin-binding GFs, the lack of specificity to bind a particular type of GF, such as heparin, limits their potential. Alternatively, short peptide sequences with biological activity similar to the biological activity of GFs may be beneficial to ascertain the therapeutic benefits of GFs. Recently, Adini et al. reported that the use of a specific VEGF binding peptide (12-mer peptide sequence) can enhance the biological activity of exogenous VEGF in vitro and in vivo to promote angiogenesis [18–20] while avoiding the potential risks of exogenously delivered or covalently tethered GFs on scaffold materials. Prominin-1-derived peptide (PR1P), a novel 12-amino acid sequence (DRVQRQTTTVVA) derived from an extracellular VEGF-binding domain of the proangiogenic glycoprotein prominin-1, can immobilize VEGF through hydrogen-bond interactions [19]. Thus, PR1P has the potential to recruit VEGF in situ at the injury site for effective tissue repair. While previous studies explored PR1P-mediated in situ VEGF binding, an elaborate mechanism detailing VEGF-mediated wound regeneration remains to be explored [10, 20].

The overarching goal of this research was therefore to design intelligent multifunctional bandages with the capability to recruit VEGF in situ at the injury site and explore VEGF-mediated angiogenesis and immune modulation for scarless wound healing. PR1P was encapsulated into biocompatible and biodegradable poly (lactide-co-glycolic acid)/gelatin (PLGA/gelatin, P/G)-based nanofibrous bandages.

Electrospinning, a versatile and cost-effective technology, could help realize the fabrication of nanofibrous bandages mimicking the extracellular matrix (ECM) morphology [21]. Unlike traditional bandages, nanofibrous bandages possess high porosity and nanoscale pores, allowing the isolation of the wound and the external environment and ensuring permeability, which can effectively promote wound healing. Meanwhile, the large specific surface area of nanofiber bandages allows for efficient drug delivery [21, 22]. Consequently, the nanofiber bandage is suitable as a wound dressing for better wound regeneration. The bandage is thus hypothesized to recruit VEGF in situ at the injury site to improve angiogenesis. Consequently, in situ VEGF recruitment and proangiogenic functions of bandages were first validated. The in situ VEGF-recruiting bandages were leveraged in splint-fixed large-sized wounds, either with or without diabetes. The structure and functions of regenerated skin were systematically evaluated, including the healing ratio, the number of hair follicles and sensory nerves and the arrangement of collagen. Moreover, RNA sequencing was performed to dissect the bandage-mediated changes in the immune microenvironment at the injury site and to validate the key regulatory axis. Taken together, these VEGF-recruiting proangiogenic bandages may offer a promising platform to meet clinical requirements, which may also be exploited for the regeneration of other tissues/organs requiring adequate angiogenesis.

Experimental Section

Fabrication of P/G-PR1P Bandages

To prepare PLGA/gelatin-PR1P (P/G-PR1P) bandages, 2 g of PLGA (LA:GA = 50:50, Mw = 95 kDa, Jinan Daigang Biomaterial Co., Ltd., Jinan, China) and gelatin (Gel, Type B, 48,722-500G-F, Sigma Aldrich, Shangahi, China) (7:3, w/w) were dissolved in 20 mL of hexafluoroisopropanol (HFIP, 99.5%, Shanghai Darui Fine Chemical Co., Ltd., Shanghai, China) to afford 10% (w/v) solution of P/G. To accurately incorporate PR1P (amino acid sequence, DRVQRQTTTVVA, China Peptides Co., Ltd., Shanghai, China) into electrospinning solution, 1 mg of PR1P was mixed with 1 mL of HFIP to afford 1 mg/mL solution. Thereafter, the respective volume of PR1P solution (e.g.,

200, 20, 2 μL, etc.) was added into 20 mL of P/G solution, and named according to the content of PR1P, such as 0.2 mg PR1P (P/G-0.2 mg PR1P), 0.02 mg PR1P (P/G-0.02 mg PR1P), and 0.002 mg PR1P (P/G-0.002 mg PR1P). Random electrospun nanofibers were fabricated by electrospinning (Yongkang Leye Technology Development Co., Ltd. SS-3556H, Beijing, China). The electrospinning parameters were as follows: Needle size, 21G, flow-rate 2.0 mL/h; voltage, 10.0 kV; distance between the tip of the spinneret and the drum collector (diameter, 100 mm), 10 cm; and collector speed, 120 rotations per minute (rpm). Electrospinning was continued for up to 3.5 h at ambient temperature (~ 25 ℃) and relative humidity was in the range of 45−50%. Electrospun bandages (thickness, 0.15−0.30 mm) were dried under vacuum and stored for the subsequent use.

Morphological Characterization

The morphology of the bandage was assessed by using field emission scanning electron microscopy (SEM, JSM-7001F, JEOL, Japan) after coating with a thin gold layer by using an auto sputter fine coater (JFC 1600, JEOL, Tokyo, Japan) before imaging. Twenty representative images were chosen ($n = 5$ independent prints) and the diameter of the fibers was determined by using ImageJ software (version 1.8). Three 3000× magnification SEM micrographs of each bandage group were randomly selected, and five fields of view of the same size were selected from each image, in which the diameters of a total of 100 nanofibers were measured by ImageJ to analyze the diameter distribution.

Water Contact Angle

The water contact angle (WAC) of scaffolds was measured by the contact angle instrument (DSA 100, Krüss, Germany) with a 3 μL liquid droplet. The contact time between the water droplets and the scaffold was recorded as 0 s. The pictures of the samples for up to the disappearance of the water droplets were continuously collected. Image J software was used for the assessment of WAC of scaffolds ($n = 3$).

Thermogravimetric Analysis

The thermogravimetric analysis (TGA) of bandages was carried out by using a Thermogravimetric Analyzer (PerkinElmer Enterprise Management (Shanghai) Co., Ltd., TGA8000, Shanghai, China). The analysis was carried out at a heating rate of 15 ℃/min from room temperature for up to 800 ℃. The thermogravimetric parameters, including maximum degradation temperature (T max) were analyzed by the TGA curves.

Porosity

The total porosity (P) of scaffolds was determined by using a liquid displacement method. Samples were prepared into rectangular shapes ($20 \times 20 \times 0.25$ mm) and weighed (W0). Afterwards, scaffolds were transferred into absolute ethanol for up to 3 h and then placed on the filter paper to remove the residual ethanol. The weight of the scaffolds was recorded as W1. The porosity of scaffolds was determined by Eq. 1:

$$P = \frac{(W_1 - W_0)}{(\rho \times V)} \times 100 \qquad (1)$$

where W_0 and W_1 represent weight of the scaffolds before and after soaking in ethanol, respectively, ρ represents the density of the ethanol at room temperature, and V the volume of the wet scaffold ($n = 5$).

Mechanical Properties

The tensile properties of P/G-PR1P bandages (30×10 mm) were evaluated in wet state by using a universal tensile testing machine (Instron-5542, Canton, USA) with a 200 N load cell (Transcell Technology, Inc., BAB-20MT, USA). All specimens were immersed in PBS for up to 10 min before tensile test. An adhesive paper was used (10 mm on both ends) to fix samples into the grips. All samples were evaluated at a fixed rate of 5 mm/min at room temperature until failure ($n = 5$). The ultimate tensile strength (UTS) was calculated from the maximum load before failure and the Young's modulus (E) was calculated from the linear region of stress–strain curve ($n = 5$).

Incorporation of PR1P into bandages

The fluorescence intensity of P/G-PR1P bandages fabricated by using different concentrations of rhodamine-labelled PR1P (e.g., 0.002, 0.02, and 0.2 mg/mL etc.) was detected by confocal laser scanning microscopy (CLSM, SP8confocal, Leica, Germany). Images were collected by using the same parameters at the scanning depth of 0.1−0.3 mm of scaffold thickness. The Zeiss ZEN software (ZEN 2.3, blue version) was used to calculate the fluorescence intensity of three random square sites (20×20 μm) of the collected pictures ($n = 3$).

VEGF Recruitment In Vitro

About 2 nano grams of VEGF was dissolved in 10 mL of standard diluent to afford VEGF solution with a concentration of 0.2 ng/mL. The P/G-PR1P bandages (5×5 mm)

containing different concentrations of PR1P (e.g., 0.002, 0.02, and 0.2 mg/mL, etc.) were immersed in VEGF solution at 37 ℃ for up to 2 h. Afterwards, bandages were rinsed with deionized water three times to obtain VEGF-bound bandages. Subsequently, bandages ($n = 5$) were transferred to a 1.5 mL Eppendorf tube, and 1 mL of standard diluent was added. The bandages were incubated for up to 12 h to facilitate VEGF release at 37 ℃. The VEGF release was studied by using a Rat Vascular Endothelial Growth Factor ELISA Kit (Solarbio, China). The optical density (OD) of samples was measured by an ELISA plate reader (Thermo Fisher Technology (China) Co., Ltd., 1,410,101, Multiskan™ FC, Shanghai, China) at 450 nm.

Biocompatibility of Bandages In Vitro

Human foreskin fibroblasts (HFF-1), RAW macrophages and human umbilical vein endothelial cells (HUVECs) (Procell Pricella, Wuhan, China) were cultured in Dulbecco's modified eagle medium (DMEM) supplemented with 100 U/mL penicillin, 100 U/mL streptomycin, 0.1 mg/mL streptomycin, and 15% fetal bovine serum (FBS) in an incubator at 37 ℃ and 5% CO_2. The bandages of appropriate size were placed in 24-well cell plate and were washed with deionized water. Subsequently, the bandages were washed with PBS twice for up to 15 min. The HFF-1 cells (1.0×10^4, cells/well) were seeded onto the surface of the bandages and incubated at 37 ℃, 5% CO_2 for up to 1, 3, 5, and 7 days. At each time point, cell proliferation was assessed by cell counting kit-8 (CCK-8, C0038, Beyotime, China). The OD values of samples were measured at 450 nm by an ELISA plate reader (Epoch™, BioTek, USA) at 450 nm ($n = 3$). For morphological analysis, the scaffolds were dehydrated with the graded ethanol series and sputter-coated with gold at 5 mA for up to 60 s and observed by SEM (Phenom ProX, Netherlands).

Scratch Wound Healing Assay

HUVECs and HFF-1 cells were grown for up to 70−80% confluence in a six-well tissue culture plate and were treated with 50 nmol/mL mitomycin for 4 h and then washed twice with sterile PBS. The cell monolayer in each well was then scratched with a sterile plastic tip, and the cells were washed twice with PBS and incubated in medium along with the extract solution of PR1P-VEGF bandages for up to 12 h. The cells and wound were imaged at 0, 6, 12, and 24 h, and the area of wound closure was calculated with ImageJ 1.8 software (National Institutes of Health) for three independent replicate experiments.

Tube Formation Assay In Vitro

The Matrigel™ (catalogue # 356,234, Corning, USA) was prepared at 0 °C overnight. About 50 μL of the Matrigel was added to a pre-cooled 96-well plate and incubated at 37 °C, 5% CO_2 for up to 30 min. For tubular formation assay, HUVECs 1.5×10^4 cells per well were cultured in a 96-well plate containing Matrigel and 100 μL of the extract solution and were incubated for 6 h. The formation of the capillary-like structure was observed through a light microscope (Olympus IX73; Olympus, Tokyo, Japan). The network parameters of the capillary-like structures, such as the nodes, total branching length, and circles were analyzed and quantified by using Image J (File-open-Angiogenesis Analyze and Analyze HUVEC Phase Contrast) (NIH, v1.8.0, USA) ($n = 3$).

Full-Thickness Splinted Excisional Wound in a Normal or Diabetic Rat Model

10-week-old Lewis-rats were supplied by SLACCAS (Shanghai, China) and maintained in the Tongji University Animal Center. All animals were maintained in specific pathogen-free conditions in microisolator cages and were treated by following the guidelines for the care and use of animals (National Research Council and Tongji University). The procedures for the care and use of animals were approved by the Ethics Committee of Shanghai Pulmonary Hospital (Shanghai, China) and all applicable institutional and governmental regulations concerning the ethical use of animals were followed.

The bandages were evaluated by using a splinted excisional wound model in Lewis-rats and diabetic Lewis-rats (male, 10 weeks old, SLACCAS, Shanghai, China). Rats were randomly divided into five groups: (a) Untreated control (splinted-only; $n = 5$), (b) P/G ($n = 5$), (c) P/G-0.002 mg PR1P ($n = 5$) (d) P/G-0.02 mg PR1P ($n = 5$), and (e) and P/G-0.2 mg PR1P ($n = 5$). Anesthesia was induced with 1% sodium pentobarbital during surgery. In each animal, two skin wounds were created in the dorsal skin by using a sterile, disposable 15.0 mm biopsy punch tool (Acu-punch; Acuderm, USA, Catalogue Number: CE0413). The wounds were stented with custom-made silica gel splints (diameter, 15 mm) and were wrapped up with different bandages. Rats were housed individually post-operation with access to food and water ad libitum. A dose of analgesic was given immediately after surgery (buprenorphine 0.1 mg/kg, subcutaneous; every 6 h for 24 h). Animals were housed under SPF conditions for 18 days, and the bandages were changed twice a week.

Measurement of Wound Area

The digital photographs were used to monitor the wound closure over time and were taken at 1, 3, 7, 10, 14, 18 days post implantation. A ruler was placed adjacent to the wound to provide a reference for measuring the area of the wound. Photographs were analyzed by ImageJ software and the wound area was determined.

Histological and Immunohistochemical Analysis

Animals were euthanized at different time points and the wound tissues (regenerated skin within the silicone silica gel range) were harvested. Specimens were fixed in 4% paraformaldehyde for 24 h followed by PBS washing and incubation in 70% (v/v) ethanol until further analysis. The specimens were dehydrated with a graded ethanol series and embedded in paraffin. Then, 8 μm thick sections were obtained and analyzed by using hematoxylin and eosin (H&E) and Masson's trichrome staining. Sections were also stained with anti-CD31 (ab182981, Abcam, UK), anti-α-SMA (ab108595; Abcam), anti-CD86 (ab97585; Abcam), and anti-CD206 (CD206, ab182422, Abcam) antibodies by using standard immunofluorescent (IF) staining procedures. ImageJ software was used to quantify the number of positive cells or positive areas in each field of view.

Microfil Perfusion and Micro-CT

Lewis-rats were perfused with Microfil (MV-122; Flow Tech, USA), and neovascularization was evaluated 7 and 14 days after surgery. The experimental animals were euthanized and were then perfused intracardially with 100 mL of heparinized saline, and 20 mL of Microfil was continuously injected at 2 mL/min. The dye entered the neovascularized area of the wound through the cardiac vessels. Finally, the experimental samples were incubated in a polymerizing contrast agent at 4 ℃ overnight. On the next day, the wound samples were sectioned by using micro-CT instrument (Pingsheng Technology Company, China). Red colour indicated the new blood vessels. SkyScan software (SkyScan Company) was used to reconstruct 3D images of wound neovascularization. The same section was selected, and neovascularization was marked in red in the figure. The number of new blood vessels per unit area as well as the area occupied by new blood vessels were calculated, and the data for both groups were analyzed with ImageJ software.

RNA-Sequencing and Data Analysis

RNA-Sequencing was performed by using standard sequencing procedures (Cloud-seq Company, China). Agene was considered to be expressed in a sample if its value was equal to or greater than that of 1 in the sample. Differentially expressed genes (DEGs) were defined as fold change ≥ 4 and P value ≤ 0.05. Gene ontology analysis was performed by using DAVID and REVIGO (https://david.ncifcrf.gov; http://revigo.irb.hr/). Target gene screening was based on GeneCards dataset (https://www.genecards.org/). For each group, 3 duplicates were collected and their RNAs were extracted, sequenced, and analyzed.

Western Blot Analysis

Neo-skin tissues were washed two to three times with cold PBS to remove blood stains and were cut into small pieces. The total proteins was extracted in RIPA Lysis Buffer (Beyotime Institute of Biotechnology, China), which contains protease inhibitor cocktails (Bimake, Houston, TX, USA), followed by centrifugation at 12,000 rpm, 4 °C, and 20 min. The protein concentration of the supernatant was determined by bicinchoninic acid assay (BCA, Pierce, Appleton, WI, USA). In total, 15–30 μg of the protein lysate was loaded into a 7–15% polyacrylamide gel and transferred to a polyvinylidene fluoride membrane (Millipore). The blots were blocked with 5% BSA in TBS + 0.1% Tween20 for 1 h, and then incubated with primary antibodies against NF-κb, TNF-α, COX2, MMP9, IL-6, and β-Actin in 5% BSA overnight at 4 °C, and followed by incubation with the corresponding HRP-conjugated secondary antibodies (Proteintech, Rosemont, IL, USA) for up to 1 h at room temperature. Thermo ECL Western Blotting Detection Reagent and Gel were used for protein visualization (Thermo Fisher Scientific, USA). The blots were then reported with β-Actin antibody. Densitometric analysis of proteins was performed by Tanon 5200S (Bio-Equip, Nanjing, China). The data are representative of three independent experiments. The primary antibodies used are listed in Supplementary Table S1.

Statistical Analysis

All data are shown as the mean ± standard deviation (SD) values. Independent samples t tests were used to compare means between two groups. One-way analysis of variance (ANOVA) was used to determine the level of significance with GraphPad Prism software (8.0), and $P < 0.05$ was considered to indicate statistical significance. *$P < 0.05$, **$P < 0.01$, ***$P < 0.001$.
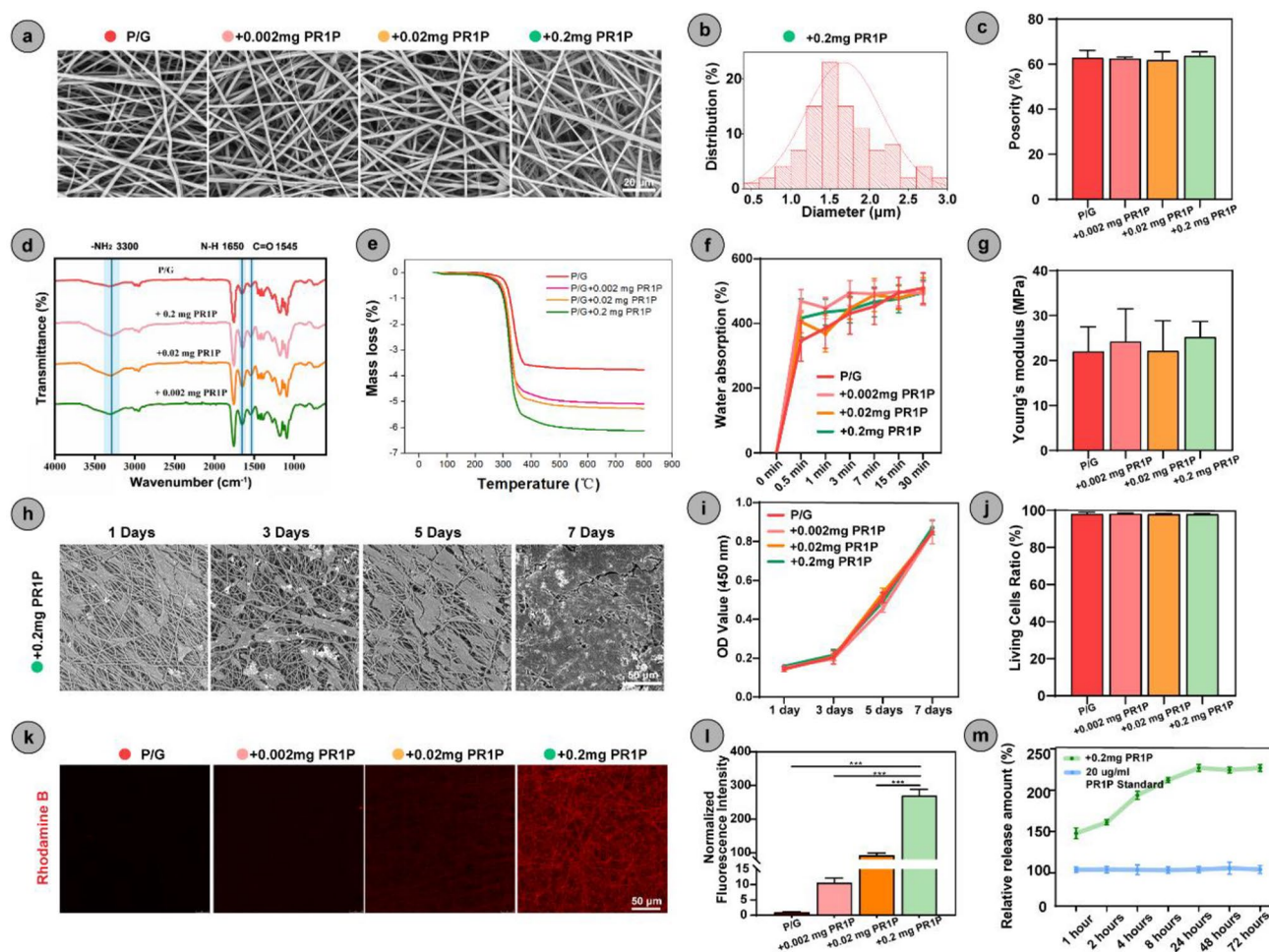
Fig. 1 Fabrication and characterization of the P/G-PR1P bandages. **a** SEM images of the P/G-PR1P bandages. Scale bar, 20 μm. **b** Diameter distribution of the P/G-0.2 mg PR1P bandage. **c** Porosity (red, pink, orange and green represent P/G, P/G-0.002 mg PR1P, P/G-0.02 mg PR1P, and P/G-0.2 mg PR1P bandages, respectively). **d** FTIR spectrum. **e** TG curve. **f** Water absorption. **g** Young's modulus. **h–j** Proliferation and morphology of HFF-1 cells on P/G-PR1P bandages in vitro. **h** SEM images of HFF-1 cells on P/G-0.2 mg PR1P bandages on Days 1, 3, 5, and 7. Scale bar, 20 μm. **i** CCK-8 proliferation curve. **j** Proportion of living cells in a live-dead staining assay. **k–l** Validation of the PR1P concentration encapsulated in the P/G-PR1P bandages. **k** Representative fluorescence images of the P/G-PR1P bandages. Scale bar, 50 μm. **l** Quantification of the fluorescence intensity ($n=3$). **m** Relative release amount of PR1P ($n=3$). $*P<0.05$, $**P<0.01$, and $***P<0.001$

Results

Encapsulation of PR1P into P/G nanofibers to Fabricate VEGF-Recruiting Bandages

PR1P was encapsulated into P/G nanofibers by using electrospinning (Fig. 1). The morphology of the P/G-PR1P bandages was discerned by scanning electron microscopy (SEM) (Fig. 1a). SEM micrographs displayed the formation of bead-free uniform nanofibers, indicating that PR1P was uniformly encapsulated into the membranes. The average diameter of the fibers was 1.61 ± 0.49, 1.69 ± 0.43, 1.69 ± 0.53, and 1.67 ± 0.48 μm for the P/G, P/G-0.002 mg PR1P, P/G-0.02 mg PR1P, and P/G-0.2 mg PR1P nanofiber

bandages, respectively (Fig. 1b, Fig. S1a, Supporting Information). The porosity of the bandages was 62.8 ± 3.0, 62.5 ± 0.6, 61.8 ± 3.3, and 63.6 ± 1.7 for the P/G, P/G-0.002 mg PR1P, P/G-0.02 mg PR1P, and P/G-0.2 mg PR1P nanofiber bandages, respectively (Fig. 1c). Fourier transform infrared spectroscopy (FTIR) revealed similar bands in the P/G and P/G-PR1P blends, indicating the blending of PR1P into P/G nanofibers (Fig. 1d).

Moreover, nanofiber bandages exhibited good biodegradability (Fig. 1e, Fig. S2, Supporting Information), water absorption (Fig. 1f), mechanical properties (Fig. 1g, Fig. S1b, Supporting Information), and biocompatibility (Fig. 1h−j, Fig. S1c-e, Supporting Information).

Next, the incorporation of PR1P as well as its release from the bandages were evaluated. Since PR1P was prelabelled with rhodamine B, confocal laser scanning microscopy (CLSM) was used to discern its encapsulation into bandages (Fig. 1k). Quantitative analysis revealed an increase in the fluorescence intensity with an increase in the PR1P concentration, indicating the successful incorporation of PR1P into nanofibers (Fig. 1l). In addition, high-performance liquid chromatography (HPLC) showed a continuous release of PR1P for up to 72 h in vitro (Fig. 1m).
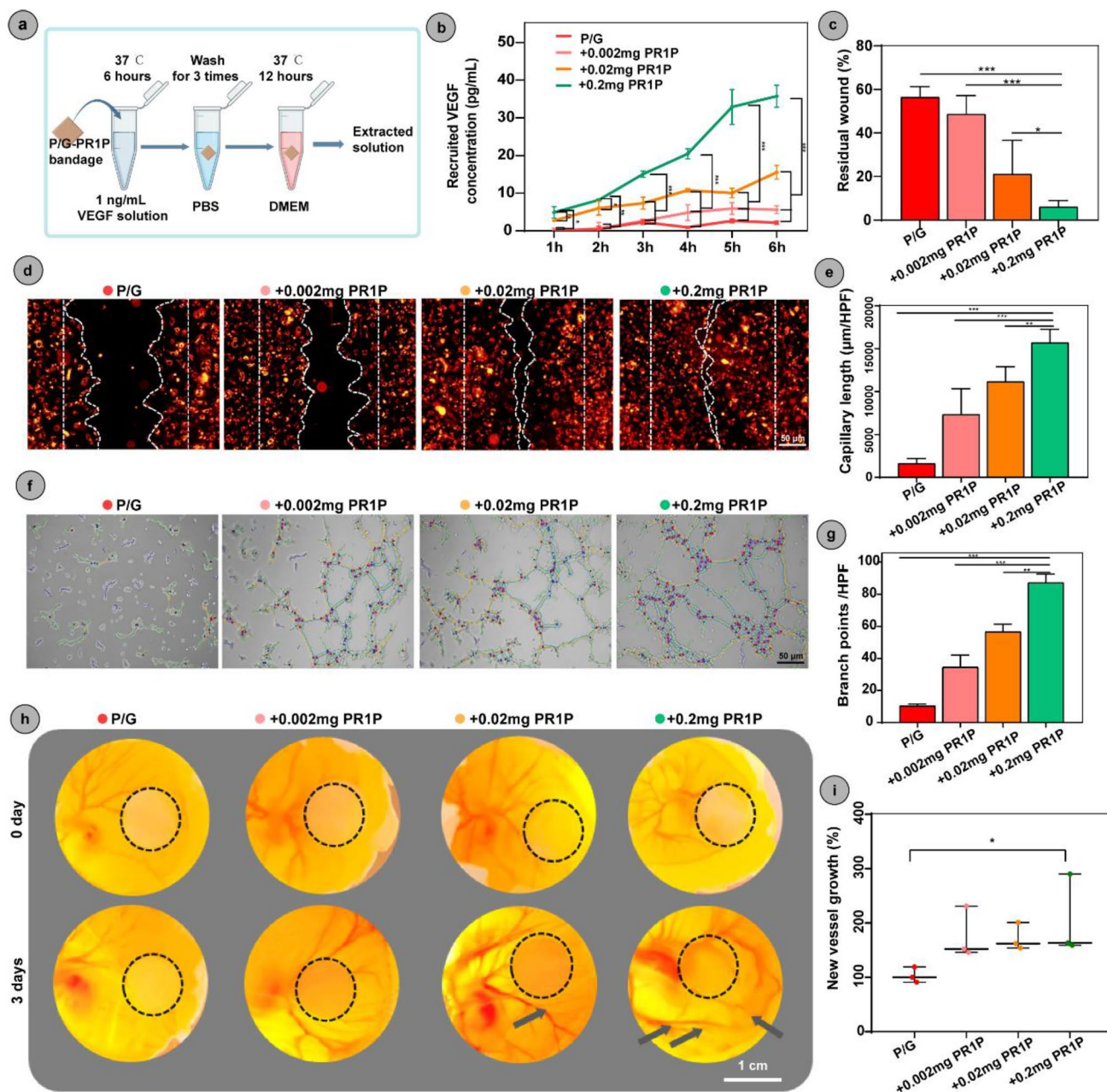
Fig. 2 P/G-PR1P bandages recruited functional VEGF in vitro. **a** Schematic illustration of mimicking in vivo VEGF recruitment and harvesting bandage extract solution. **b** Quantification of the VEGF that was recruited by P/G-PR1P bandages ($n=3$). **c–d** Bandage-recruited VEGF promoted HUVEC migration. **c** Representative migration images of HUVECs stained with Celltracker-Dil (red) ($n=3$). Scale bar, 50 μm. **d** Quantitative analysis of the migration of HUVECs. **e–g** Bandage-recruited VEGF promoted tube formation. **e** Quantitative analysis of capillary length ($n=3$). **f** Representative images of the tube formation assay in HUVECs ($n=3$). Purple dots indicate the structure of branch points. Scale bar, 50 μm. **g** Quantitative analysis of the number of branch points ($n=3$). **h** Chick embryonic experiment for testing the angiogenic potential of P/G-PR1P bandages. Arrows represent new vessel growth. **i** Quantitative analysis of new vessel growth in chick embryos. *$P<0.05$, **$P<0.01$, and ***$P<0.001$

P/G-PR1P Bandages Induced a Functional VEGF Peak In Vitro

To demonstrate that the P/G-PR1P bandages, consistent with the hypothesis, can recruit endogenous VEGF and thus form VEGF peaks locally, the recruitment ability of VEGF was first validated in vitro (Fig. 2a).

The bandages were incubated in a pre-established concentration of VEGF solution, and the recruited VEGF was extracted for up to 6 h. The extracts were then analyzed by enzyme-linked immunosorbent assay (ELISA) (Fig. 2b, Fig. S1f, Supporting Information). All the bandages containing PR1P effectively captured VEGF in a PR1P concentration-dependent manner. The 0.5 cm^2 P/G-0.2 mg PR1P bandages recruited approximately 35.7 ± 2.9 picograms of VEGF within 6 h (Fig. 2b).

To confirm that the recruited VEGF retains its biological function, the extracts were used to induce tubular formation in vascular endothelial cells (vECs), the main cell type for angiogenesis. Scratch wound healing and tube formation assays were carried out to simulate the in vivo angiogenesis processes. As shown in Fig. 2c–g, the extracts from the PR1P bandages significantly promoted the migration of vascular endothelial cells (vECs) as well as the formation of a tubule network of vECs in vitro. The wound closure rate of the P/G-0.2 mg PR1P group was significantly higher than the wound closure rate of the other groups, which indicated that PR1P acted in a concentration-dependent manner (Fig. 2c−d and Fig. S3a, Supporting Information). The tubule network formation assay using human umbilical vein endothelial cells (HUVECs) also demonstrated an obvious angiogenic effect in the P/G-PR1P groups compared with the P/G group (Fig. 2f and Fig. S3b, Supporting Information). Quantitative analysis further revealed significantly higher capillary length and branch points in the P/G-PR1P bandages than in the P/G bandages (Fig. 2e–g).

P/G-PR1P Bandages Promoted Angiogenesis In Vivo

As a proof-of-concept to delineate that PR1P can recruit the endogenous VEGF peak to mediate angiogenesis, a chick embryo experiment was performed, which revealed significantly higher neovascularization in the P/G-0.2 mg RP1P group than in the other groups (Fig. 2h−i).

Next, the potential of these bandages was assessed in splint-fixed full-thickness 1.5-cm-diameter excisional wounds in the dorsal skin of Lewis rats. (Fig. 3a, Fig. S4a, Supporting Information). The wounds were treated with P/G or P/G-PR1P bandages twice per week until Day 18, the time point by which wound healing was achieved in all groups except the splint-only group.

Immunofluorescence (IF) staining for CD31 and alpha-smooth muscle actin (α-SMA) was performed to evaluate the degree of angiogenesis in the wound area at Days 7, 14, and 18. In addition, angiography was performed with microCT at Days 7 and 14 to ascertain the functionality of the neovessels (Fig. 3a). The neovascularization rate was found to be increased at Days 7 and 14 posttreatments; the P/G-0.2 mg PR1P group displayed significantly higher vessel volume and vessel thickness as well as more CD31-positive and α-SMA-positive vessels than the P/G group (Fig. 3b). Three-dimensional reconstruction of angiograms showed the formation of functional subcutaneous vessels; the P/G-0.2 mg PR1P-treated group exhibited mature vascular network formation at both time points (Fig. 3c–g and Movie. S7, Supporting Information).

P/G-PR1P Bandages Enhanced Multifunctional Wound Regeneration by Promoting Hair Neogenesis, Neurogenesis, and Collagen Remodeling

Wound closure with bandages mimicking skin architecture results in less scar tissue development [23, 24]. To further explore the in vivo performance of the P/G-PR1P bandages, a thorough assessment of wound regeneration was conducted (Fig. 4a).

The wounds treated with P/G-0.2 mg PR1P bandages showed significantly less residual wound area than the control groups (splint-only and splint with P/G bandages) as well as the other low-dose PR1P groups (the P/G-0.002 mg and P/G-0.02 mg PR1P bandages). The wounds treated with P/G-0.2 mg PR1P bandages were fully healed by Day 14 (Fig. 4b–c). Histological analysis of tissue sections from the P/G-0.2 mg PR1P group revealed de novo regeneration of scarless neo-tissues as well as a higher epidermal layer and skin thickness (Fig. 4d−e).

The secretory function and tactile sensation of the neotissues were also evaluated. The healed wounds showed an abundance of immature hair follicles (Fig. S5, Supporting Information). With an increase in the treatment time, the hair follicles and glands matured, thereby resembling corresponding structures in the native skin (Fig. 4e and Fig. S5, Supporting Information). The presence and development of hair follicles and glands in Lewis rats suggested embryonic-like tissue regeneration as well as reconstruction of the secretory function of the skin, a phenomenon not often observed in large wounds, especially in rat models (Fig. 4f, Fig. S5, Supporting Information). Additionally, immunofluorescence staining for TrPV1 and other compounds confirmed a significantly higher neurogenesis rate in the P/G-0.2 mg PR1P bandage group (Fig. 4g). The Von Frey touch-test revealed the sensitivity of de novo skin to mechanical stimulation (Fig. 4h).

Barrier function and scar formation were then evaluated. The scar length, collagen deposition, and collagen
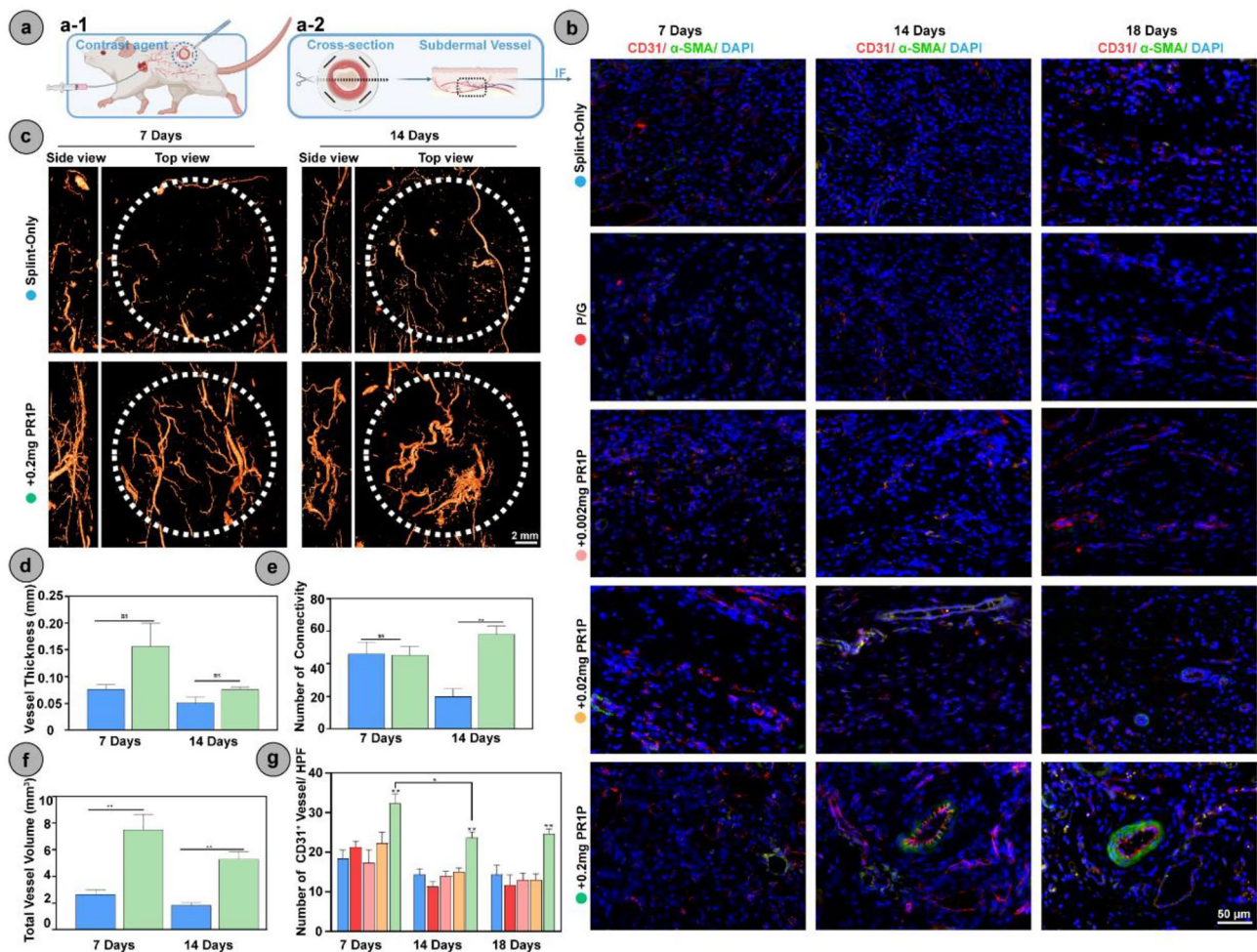
Fig. 3 P/G-PR1P bandages recruited VEGF and promoted angiogenesis in vivo. **a** Schematic illustration of angiography (a-1) and immunofluorescence (a-2). **b**–**g** Analysis of angiogenesis. **b** Immunofluorescence staining of CD31 (red) and α-SMA (green) at Days 7, 14, and 18 ($n=3$). Scale bars, 50 μm. **c** Reconstructed 3D angiography images ($n=3$). **d**–**f** Quantification of the vessel thickness (**d**), connectivity number (**e**), and total vessel volume (**f**). **g** Quantification of CD31$^+$ vessel number ($n=6$)

distribution were identified by Masson's trichrome staining. The P/G-0.2 mg PR1P group showed less scar tissue formation and the formation of native-like grid collagen networks [25] (Fig. 5a–c). Sirius red staining and pseudocolour analysis revealed the collagen direction, which was more regular and orderly in the P/G-0.2 mg PR1P group (Fig. 5d–g). Importantly, the collagen I/III ratio (green area/purple area in the pseudocolour analysis [26, 27]) in the P/G-0.2 mg PR1P group was more similar to the collagen I/III ratio in the normal skin than to the collagen I/III ratio in the other groups (Fig. 5h–i). The other groups displayed typical scar tissue with a large number of isotropic horizontally oriented collagen bundles and an irregulated epidermis, few hair follicles, sebaceous glands, or peripheral nerves (Fig. 5h and Fig. S6, Supporting Information).

RNA-Seq Revealed the Changes in the Immune Microenvironment Induced by P/G-PR1P Bandages

RNA sequencing was performed to further probe the angiogenic and immunomodulatory properties of PR1P-containing bandages.

For global assessment of the wound microenvironment after treatment with the P/G-0.2 mg PR1P bandage, whole transcriptome RNA sequencing (RNA-Seq) was performed on samples collected from wound tissues at Day 14. Tissues from wounds treated with splint-only and P/G were used as controls ($n=3$). A significant difference between the transcriptome profiles of the control and P/G-0.2 mg PR1P-treated groups was observed in a differentially
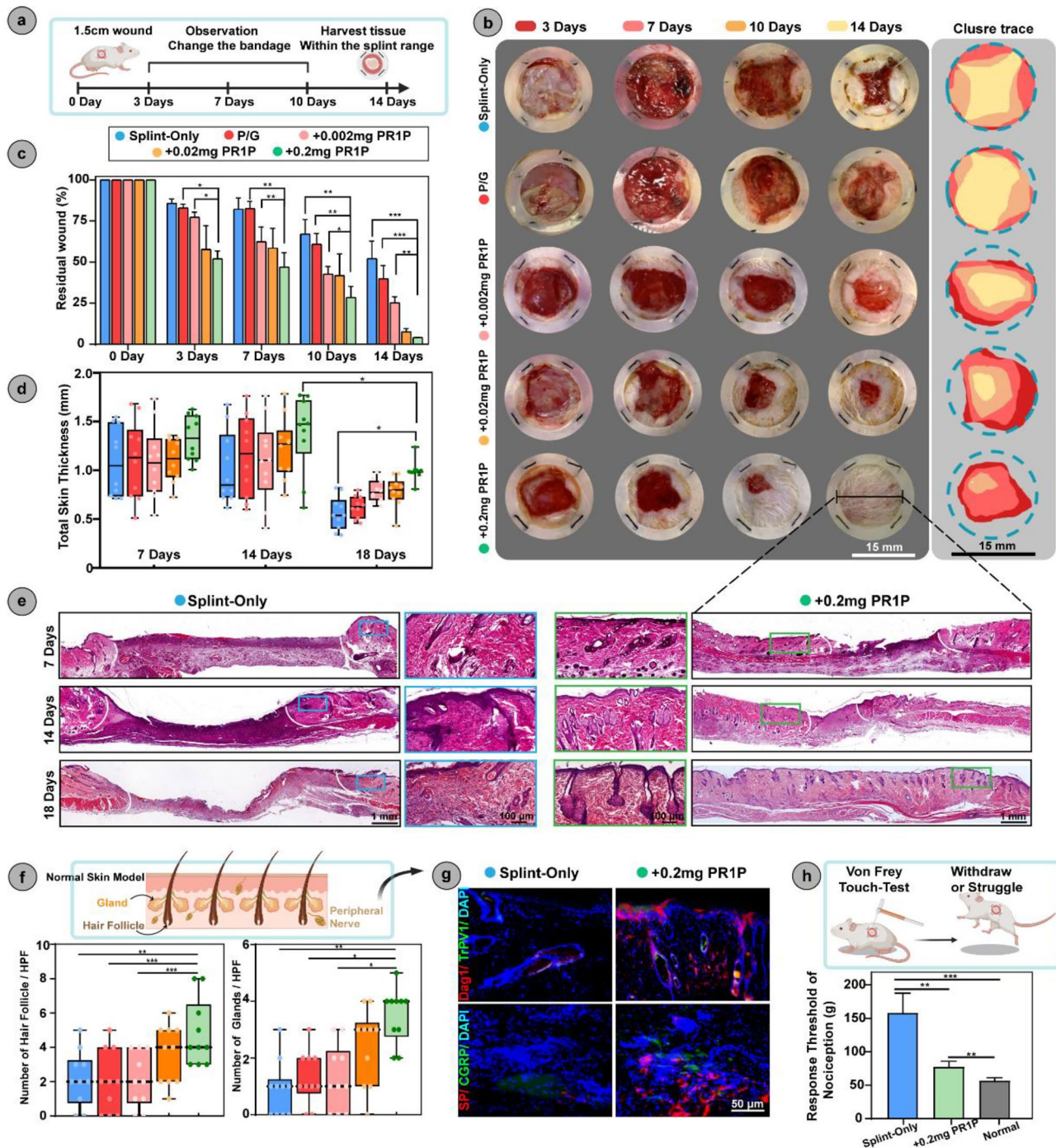
Fig. 4 P/G-PR1P bandages enhanced multifunctional wound regeneration in large splinted wounds. **a** Schematic illustration showing the animal experiments performed to test the therapeutic effect of the P/G-PR1P bandages in a Lewis rat model with a splint-fixed full-thickness 1.5-cm-diameter excisional wound model. **b–d** Analysis of wound closure. **b** Representative images and closure traces of wounds treated with or without P/G bandages and P/G-PR1P bandages for 14 days. Scale bar, 15 mm. **c** Residual wound area change during 14 days postwounding. Wound size at each time point was normalized to Day 0 ($n=6$). **d** Quantification of the mean skin thickness at the wound site ($n=6$). **e–f** Analysis of the secretory function. **e** Rep-resentative H&E staining images and magnified images of full-length skin sections within the area of the splint at 7, 14, and 18 days. Scale bars, 1 mm and 100 μm. **f** Quantification of hair follicle and gland density in the wounds at Day 18. **g–h** Analysis of neurological function. **g** Immunofluorescence staining of Dag1 (red) along with TrPV1 (green) for tactile corpuscles and SP (red) along within calcitonin gene-related peptide (CGRP) (green) for peripheral nerves at Day 18. Scale bars, 50 μm. **h** Von Frey touch-test for testing the response threshold of nociception in neoskin ($n=6$). *$P<0.05$, **$P<0.01$, and ***$P<0.001$
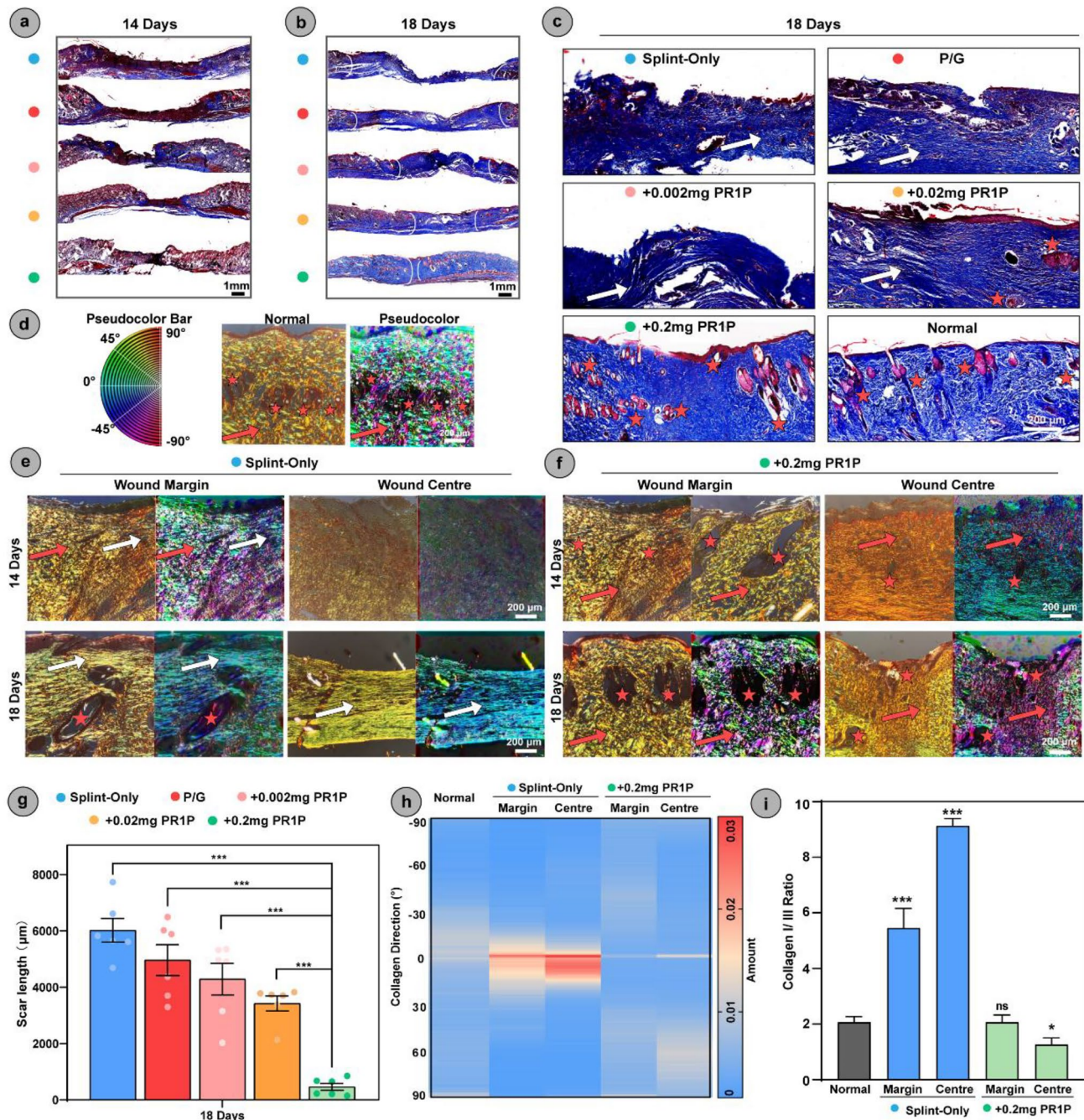
Fig. 5 P/G-PR1P bandages regulated collagen deposition in vivo. **a**–**c** Masson's trichrome staining of full-length skin sections within the area of the splint at Day 14 (**a**) and Day 18 (**b**) ($n = 6$). Scale bar, 1 mm. **c** Magnified images of the wound centre. White arrows represent horizontally oriented collagen bundles, red arrows represent basket weave-like collagen networks, and red stars represent skin appendages. Scale bar, 200 μm. **d**−**i** Analysis of the collagen arrangement. Representative images showing the collagen arrangement and pseudocolour images of the normal skin (**d**), wounds in the splinted-only group (**e**), and wounds in the P/G-0.2 mg PR1P bandage-treated group (**f**). Scale bar, 200 μm. **g** Quantification of the length of horizontally oriented collagen bundles at Day 18 ($n = 6$). **h** Heatmap of collagen proportion in different directions at Day 18. **i** Quantification of the collagen I/III ratio at Day 18. *$P < 0.05$, **$P < 0.01$, and ***$P < 0.001$
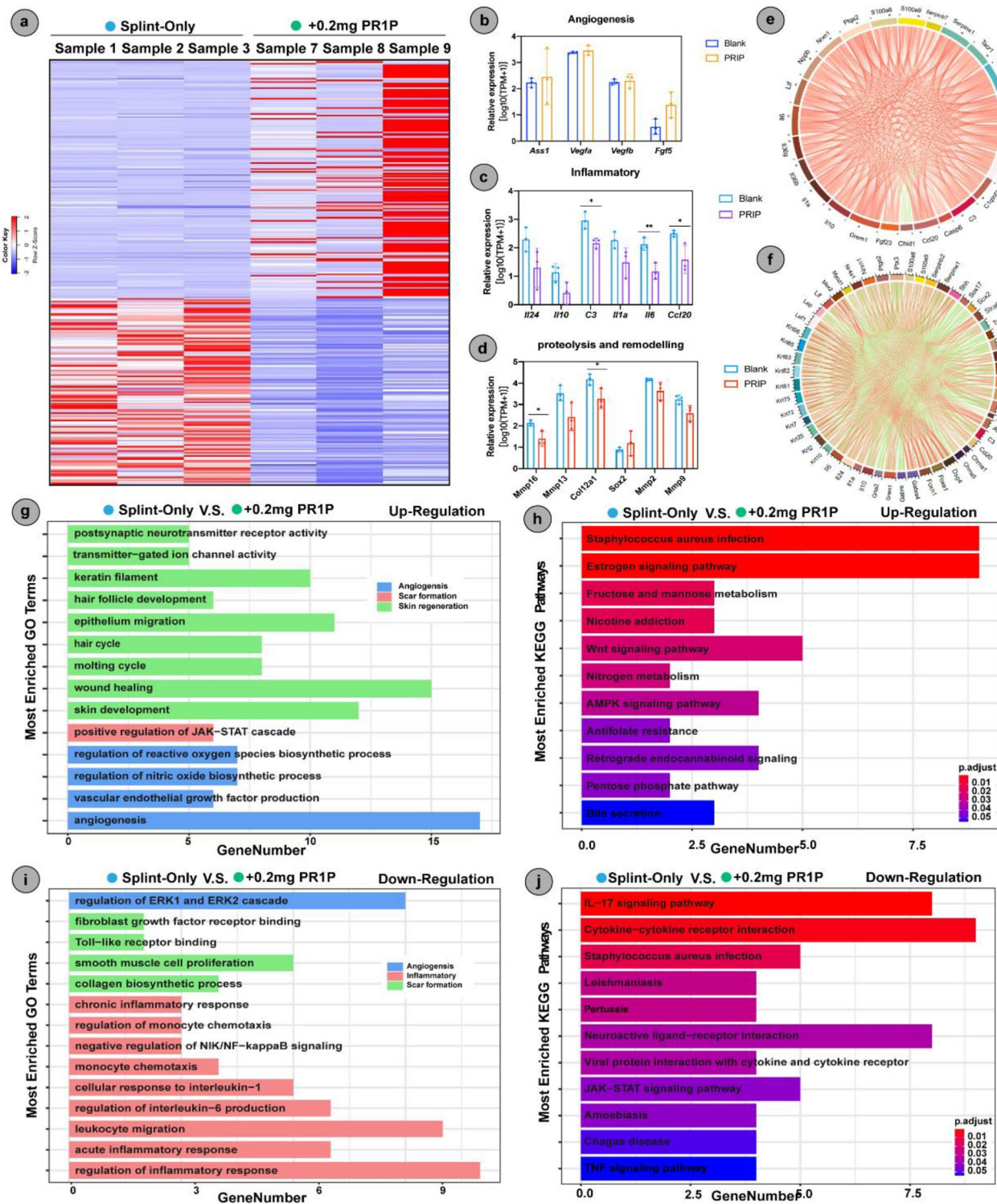
Fig. 6 Whole transcriptome RNA sequencing reveals the wound microenvironment. **a** Heatmap of upregulated and downregulated genes in the wound microenvironment after P/G-0.2 mg PR1P bandage treatment ($n = 3$, fold change ≥ 4, and $P < 0.05$). **b–d** Relative expression of genes related to the processes crucial for wound regeneration, including angiogenesis (**b**), inflammation (**c**), and remodeling (**d**) ($n = 3$). **e** String diagram of gene–gene interactions in upregulated genes. **f** String diagram of gene–gene interactions in downregulated genes. **g** Gene Ontology (GO) enrichment analysis of the upregulated genes. **h** Kyoto Encyclopedia for Genes and Genomes (KEGG) pathway enrichment analysis of the upregulated genes. **i** GO analysis of the downregulated genes. **j** KEGG analysis of the downregulated genes. *$P < 0.05$, **$P < 0.01$, and ***$P < 0.001$

expressed gene analysis (Fig. 6a and Figure S8a–b, Supporting Information).

An enrichment analysis based on differentially expressed genes was performed to identify up- and downregulated gene sets. A *t* test analysis was performed to identify differences in gene expression among the wound tissues in the splint-only and P/G-0.2 mg PR1P-treated groups (Fig. 6b–d and Fig. S8c–e, Supporting Information). Notably, the expression of genes related to angiogenesis (e.g., ASS-1, VEGF-A, VEGF-B, FGF-5, etc.) was upregulated in the P/G-0.2 mg PR1P group. However, the expression of genes related to inflammation (e.g., C3, CCL-20, IL-6, etc.), proteolysis, and scar formation (e.g., MMP9, MMP16, COL-12A1, etc.) was significantly downregulated. Gene Ontology (GO) analysis revealed that upregulated genes in the P/G-0.2 mg PR1P group were enriched in angiogenesis, regeneration of skin and its appendages, peripheral nerve regeneration, metabolism, and intracellular homeostasis. In contrast, the downregulated genes were enriched in the inflammation and fibrosis clusters (Fig. S9a-b, Supporting Information). Simultaneously, gene string diagrams and protein interactions suggested that these processes were closely interconnected (Fig. 6e–f and Fig. S10, Supporting Information).

Based on the GeneCards database, differentially expressed genes related to angiogenesis, skin regeneration, inflammation, and scar formation were identified (Fig. S10a-d, Supporting Information). A GO analysis illustrated that the aforementioned biological processes depended on the regulation of VEGF, inflammatory factors, collagen, etc. (Fig. 6g–j).

The Kyoto Encyclopedia for Genes and Genomes (KEGG) pathway enrichment analysis indicated that the P/G-0.2 mg PR1P group activated the VEGF, AMPK, oestrogen and PPAR signaling pathways, thereby enhancing angiogenesis, metabolism and intracellular homeostasis, while suppressing the interleukin-17 (IL-17), JAK-STAT, NF-κb, and TNF signaling pathways, which are associated with the polarization of macrophages and the activation of fibroblasts (Figure S9c, Supporting Information).

Three key clues were obtained by RNA-Seq. First, the P/G-PR1P bandages indeed modulated VEGF to promote angiogenesis and functional skin regeneration. Second, macrophages and fibroblasts may be influenced by the P/G-PR1P bandages and contribute to subsequent wound regeneration.

P/G-PR1P Bandages Influenced Macrophages and Fibroblasts to Realize Immunomodulatory Functions In Vivo

Interestingly, as revealed by the RNA-Seq results, macrophages and fibroblasts were influenced during the in vivo regeneration process. Therefore, specific staining of tissue sections was performed at various time points to validate the above hypotheses.

The P/G-PR1P bandages were first confirmed to facilitate macrophage polarization towards the M2 phenotype, which is important for wound regeneration. As shown in Fig. 7a–b, on Day 7, the groups did not substantially differ in terms of the number of M1 macrophages. In contrast, the P/G-0.2 mg PR1P bandage group displayed a significantly higher percentage of CD206+ (M2) macrophages than the other groups, thereby indicating that the P/G-0.2 mg PR1P bandages promoted the polarization of macrophages towards the M2 phenotype (Fig. 7c–e).

In addition, α-SMA is an essential marker for the activation of fibroblasts, indicating positive collagen deposition [28]. Immunofluorescence (IF) staining further revealed higher expression of α-SMA in the P/G-0.2 mg PR1P group (Fig. 7b). Taken together, the RNA-Seq and IF staining results suggested that the P/G-PR1P bandages exhibited immunomodulatory functions and leveraged a regenerative microenvironment.

## The Dual Function of P/G-PR1P Bandages Initiated with VEGF Recruited by PR1P

The in situ recruitment of VEGF and enhancement of VEGF function are the most critical functions of PR1P, and proangiogenic and immunomodulatory dual functions were hypothesized to be initiated by VEGF.

Therefore, we blocked VEGF and VEGF receptors (VEGFR) in vivo in the control group by administering high concentrations of recombinant VEGFR protein and anlotinib (a VEGFR inhibitor), respectively (Fig. 8a). As illustrated in Fig. 8b–e, the blockade of both VEGF and VEGFR led to poor wound healing and the loss of the regulatory effects of the bandage in the wound microenvironment (Fig. 8f–k). Specifically, angiogenesis and orderly deposition of collagen were not observed, and the infiltration of macrophages was decreased; the infiltrated macrophages exhibited a CD86+ (proinflammatory, M1) phenotype (Fig. 8j–k).

Validation at the protein level further supported these conclusions (Fig. 8f). In both the VEGF-inhibitor group and the VEGF-blocked group, the expression of inflammatory factors (NF-κb, TNF-α, PTGS2, and IL-6) and MMP-9 was increased, which indicated that the macrophages polarized towards M1, and the microenvironment progressed towards an inflammatory state rather than a regenerative state.

P/G-PR1P Bandages Exert Immunomodulatory Effects via the VEGF/Macrophage/Microenvironment Axis

The effect of P/G-PR1P bandages was finally evaluated in vitro (Fig. 9a–f), where bandages were immersed in
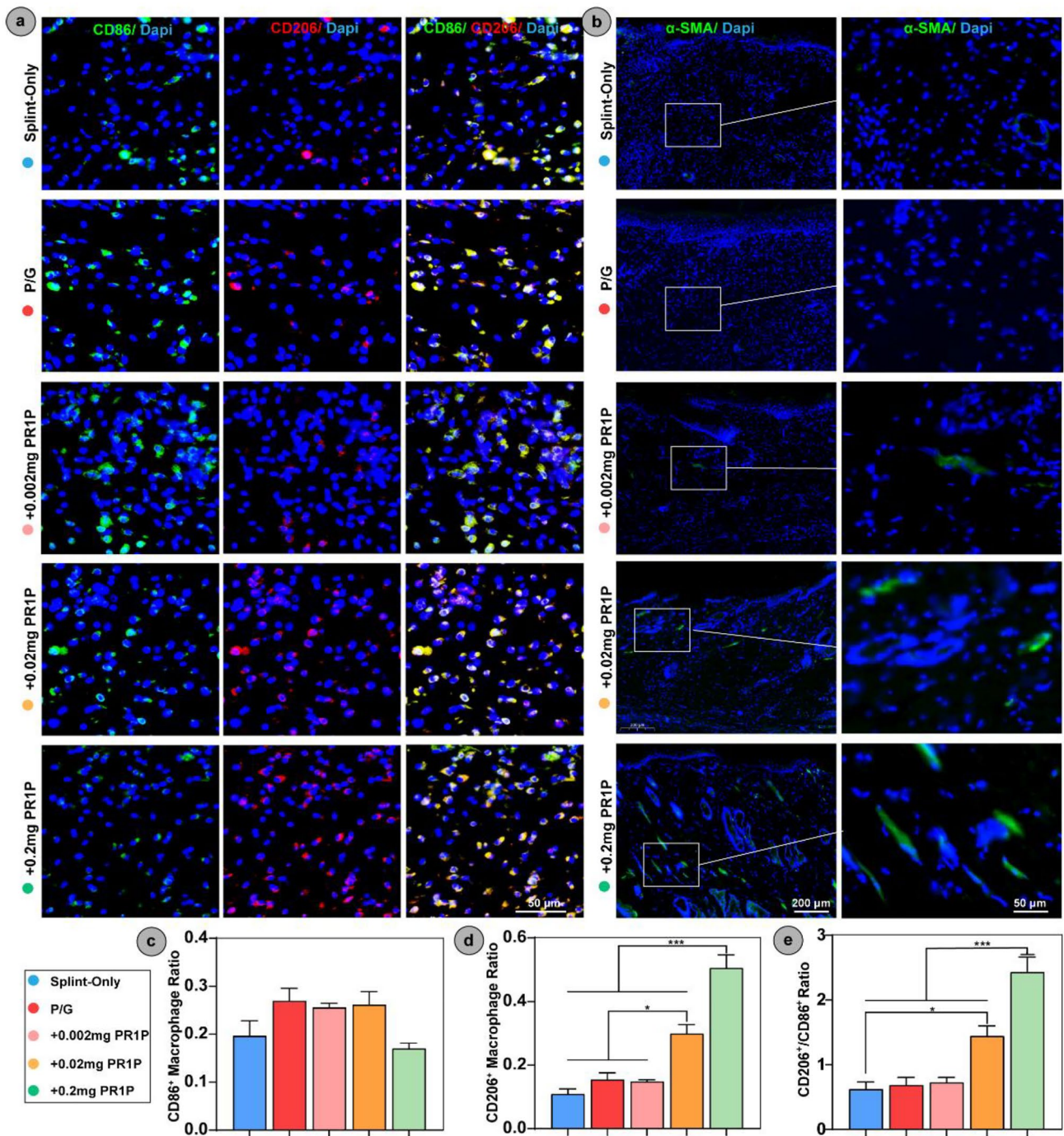
Fig. 7 VEGF-recruiting bandages regulated macrophages and fibroblasts in vivo. **a** Analysis of macrophages. Immunofluorescence staining of CD206 (red) and CD86 (green) on Day 14 ($n=3$). Scale bars, 50 μm. **b** Immunofluorescence staining images and magnification images of α-SMA (green) at Day 14 in the wound area ($n=3$). Scale bars, 200 and 50 μm. **c–e** Quantification of the CD86$^+$ macrophage ratio (**c**), CD206$^+$ macrophage ratio (**d**), and CD206$^+$/CD86$^+$ ratio (**e**). *$P<0.05$, **$P<0.01$, and ***$P<0.001$

1 ng/mL VEGF solution to simulate the endogenous VEGF recruitment process. The extract solution from the P/G and P/G-PR1P membranes was collected. Macrophages and fibroblasts, the representative cell types in which significant changes were observed in vivo, were chosen to

discern the biological effects of bandages. Interestingly, extracts were used to culture fibroblasts, and scratch experiments suggested that the extract solution of bandages displayed a minimal effect on HFF-1 cells (Fig. 9d and Fig. S3c, Supporting Information). Therefore, we hypothesized
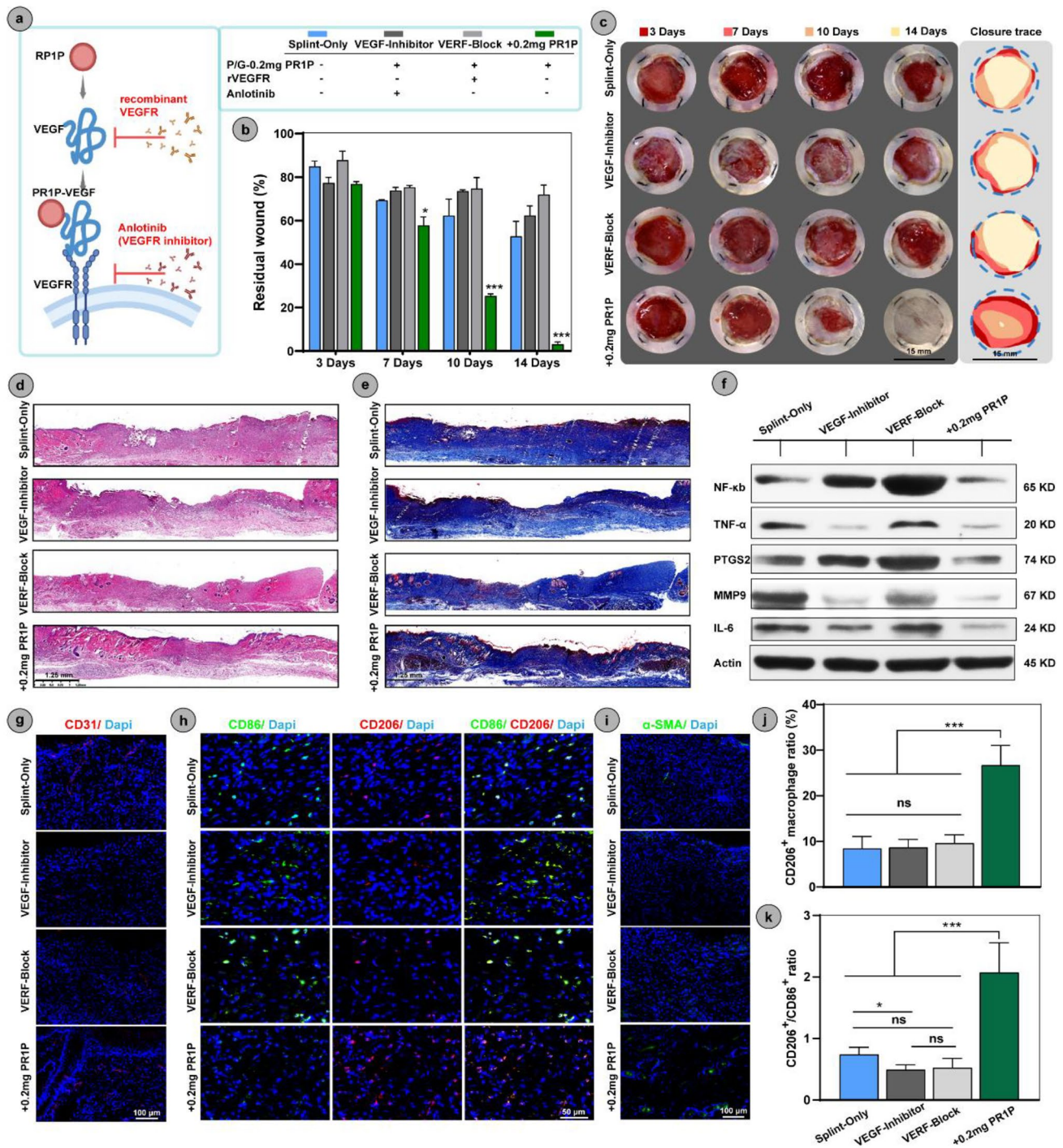
Fig. 8 The function of P/G-PR1P bandages initiated by VEGF. **a** Schematic illustration of the VEGF-block experiments. **b** Representative closure trace of the wounds treated with VEGF inhibitor or VEGF block for 14 days ($n=3$). Scale bar, 15 mm. **c** Residual wound area change during 14 days postwounding. Wound size at each time point was normalized to Day 0 ($n=3$). **d** H&E staining images of full-length sections within the area of the splint at Day 14. Scale bars, 1.25 mm. **e** Masson's trichrome staining images of full-length sec-

tions within the area of the splint at Day 14. Scale bars, 1.25 mm. **f** Immunoblotting of crucial protein expression in the wound microenvironment from the tissue lysates extracted from wounded skin at Day 14 ($n=3$). **g–i** Representative images of immunofluorescent staining at Day 14 ($n=3$). **j–k** Quantification of the CD206 + macrophage ratio (**j**) and CD206 +/CD86 + ratio (**k**). $*P<0.05$, $**P<0.01$, and $***P<0.001$
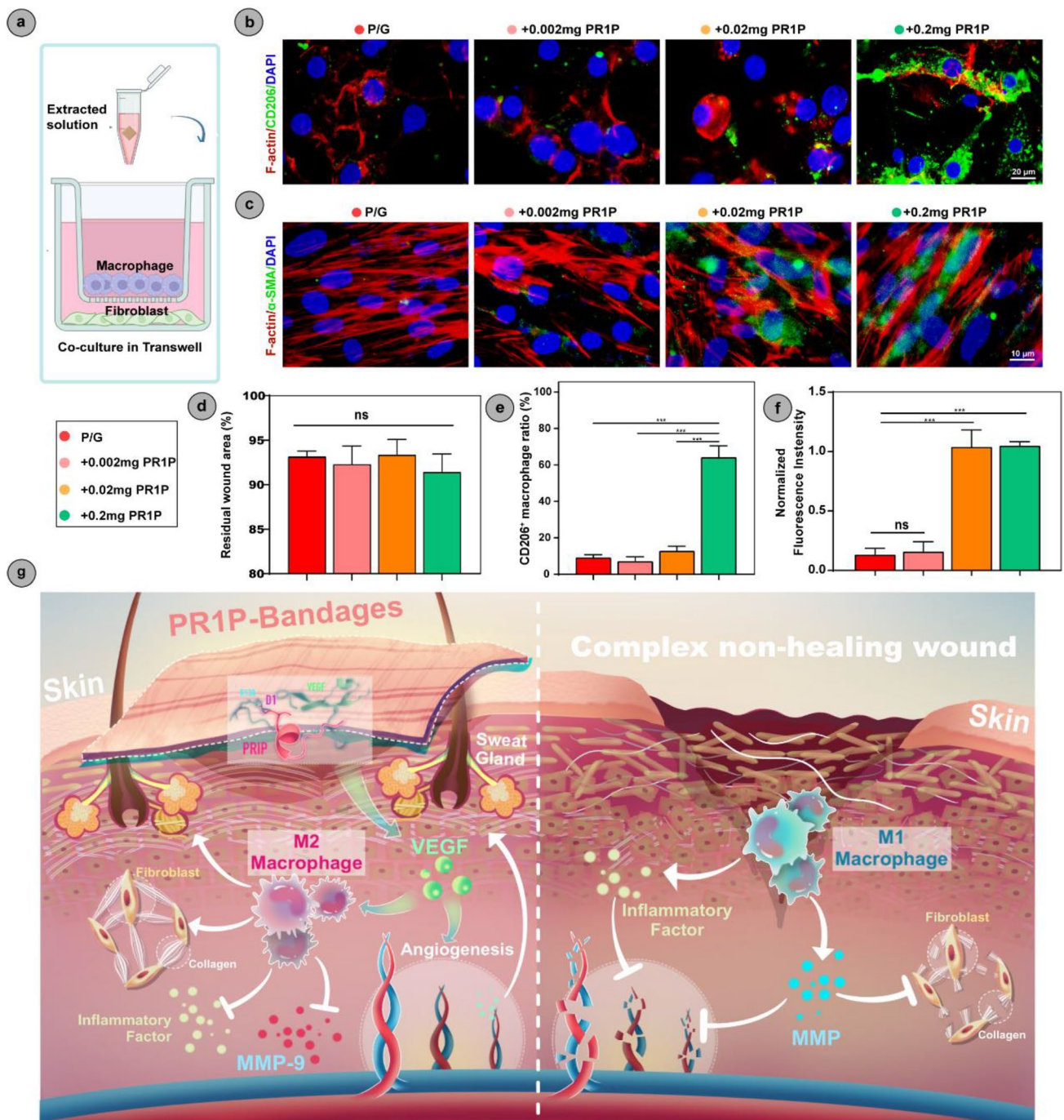
Fig. 9 The P/G-PR1P bandages exerted immunomodulatory effects via the VEGF/macrophage/microenvironment axis. **a** Schematic illustration of coculture to mimic the in vivo process. **b** Immunofluorescence staining of F-actin (red) and CD206 (green) in macrophages ($n = 3$). Scale bars, 20 μm. **c** Immunofluorescence staining of F-actin (red) and α-SMA (green) in macrophages ($n = 3$). Scale bars, 10 μm. **d** Analysis of the migration ability of HFF-1 cells after direct culture with the extracts. **e** Quantification of the CD206+ macrophage ratio. **f** Quantification of the expression of α-SMA. **g** Illustration of the mechanism. $*P < 0.05$, $**P < 0.01$, and $***P < 0.001$

that fibroblast activation was stimulated by macrophages. Thus, a Transwell coculture system was applied, in which RAW macrophages were cultured in the inner chamber, while HFF-1 cells were cultured in the outer chamber, to construct a simplified wound microenvironment. After

3 days of culture along with the extract solution of VEGF-bonded P/G-PR1P bandages, macrophages displayed plate-like pseudopods exhibiting a typical M2 morphology, along with the high expression of the representative CD206 marker for M2 (Fig. 9b−e). Meanwhile, IF staining

showed the upregulation of α-SMA expression in fibroblasts (Fig. 9f).

Altogether, multiple in vitro and in vivo validations demonstrated that peptide-modified angiogenic P/G-PR1P bandages initiated the regeneration process by endogenous VEGF. VEGF promoted neovascularization, which created a favorable metabolic environment. VEGF further promoted macrophage polarization towards the M2 phenotype, which further inhibited the expression of inflammatory factors and MMPs, activated fibroblasts and promoted collagen deposition. The two cascades amplify and form a VEGF/macrophage/microenvironment axis to promote functional tissue regeneration (Fig. 9g).

Validation of the Therapeutic Effect of the P/G-PR1P Bandages in Diabetic Wounds

Clinical situations such as diabetic wounds are often more complex [5]. Having validated the therapeutic effect of the P/G-PR1P bandage on large-sized wound models, a full-thickness dermal wound in the dorsal skin of type 2 diabetic Lewis-rat models was established to investigate the therapeutic properties of P/G-0.2 mg PR1P bandages (Fig. 10a–b and Fig. S4b, Supporting Information).

Similar results were observed in the diabetic rat model (Fig. 10c–k). The unhealed area treated with the P/G-0.02 mg PR1P bandage was reduced to 0% within 18 days (n=5). Additionally, histological analysis revealed a de novo regenerated appearance in the P/G-0.02 mg PR1P group, with more integrated epidermis coverage, more skin appendage regeneration (hair follicles and glands), orderly collagen deposition, and shorter scar length. Comparatively, wounds treated with splint-only and splint with P/G exhibited poor healing along with substantial scarring.

Preclinical Evaluation of the P/G-PR1P Bandages

Compared with traditional silk bandages, nanofiber bandages have a larger surface area, good porosity, and a higher water absorption rate, which contribute to the absorbance of wound exudate and metabolic products. In addition, these bandages exhibited a better adsorption of antibiotic solutions, as reflected by the increased width of the bacterial inhibition ring, which may also have implications for the prevention of the infection (Fig. S11a–c).

In addition, from a clinical perspective, safety is the highest priority. Histological sections of the heart, liver, spleen, lungs, and kidneys in rats of the P/G-PR1P group exhibited insignificant structural alterations compared to the control group (Fig. S11d–e), thereby demonstrating the biological safety of bandages.

Moreover, the combination of biocompatibility and low cell adhesion (Fig. S1a–d) of the P/G nanofibers (PLGA:

gelatin=7:3) prevented secondary injury during the transplantation of bandages.

Discussion

In clinical scenarios, the treatment for accelerating scarless healing of complex wounds, such as large wounds, burn wounds, and diabetic wounds, is a persistent and an unmet need [29, 30]. From the perspective of a clinician, a good wound treatment product should meet three requirements: (i) convenience of use, (ii) low cost, and (iii) excellent therapeutic efficiency [5, 31]. In terms of therapeutic efficacy, the goals of wound repair are multifaceted [1, 22, 25, 32]. For the first facet, the wound needs to be closed rapidly to restore the most basic barrier function. Second, scar formation should be inhibited. Third, at a higher level, the regeneration of skin appendages and sensory nerves should be considered, which may be pivotal to the restoration of the secretory function and nerve perception of the skin. Currently, few studies can meet these multifaceted goals for skin repair, which necessitates alternative therapeutic strategies.

Growth factors were first given attention for their key role in wound regeneration [7, 9–11, 27]. Additionally, growth factors are permitted by the Food and Drug Administration (FDA) as a mature clinical wound treatment. For example, in China, recombinant human epidermal growth factor (rhEGF) and recombinant human vascular endothelial growth factor (rhVEGF) solutions are often sprayed by clinicians on bandages to promote wound regeneration [31]. However, shortcomings of growth factors limit their clinical applicability [11, 33]. As large molecular weight proteins, growth factors exhibit a short half-life and poor retention at the wound site, which may preclude their therapeutic benefits. In addition, a high dose of exogenous growth factors may induce potential risks, including foreign body response (FBR) and potential tumor formation, which may further limit the usefulness of this approach.

Recently, nanomaterials, especially fibrous nanomaterials, have shown promising benefits for tissue repair due to their multichannel structure, biocompatibility, tunable size and controlled surface modification [34–41]. Owing to their ability to recapitulate natural ECM and promote cell growth and chemotaxis, nanofibrous scaffolds have been used for different types of biomedical applications, such as wound healing and drug delivery [40–43].

In this study, PR1P was encapsulated into nanofibers to fabricate VEGF-recruiting nanofiber bandages (P/G-PR1P bandages) to enhance multifaceted functional skin regeneration. PR1P, a 12-amino acid peptide sequence, specifically potentiates VEGF in situ and augments VEGF signaling within local wound microenvironments [19]. The encapsulation of PR1P into nanofibers enables
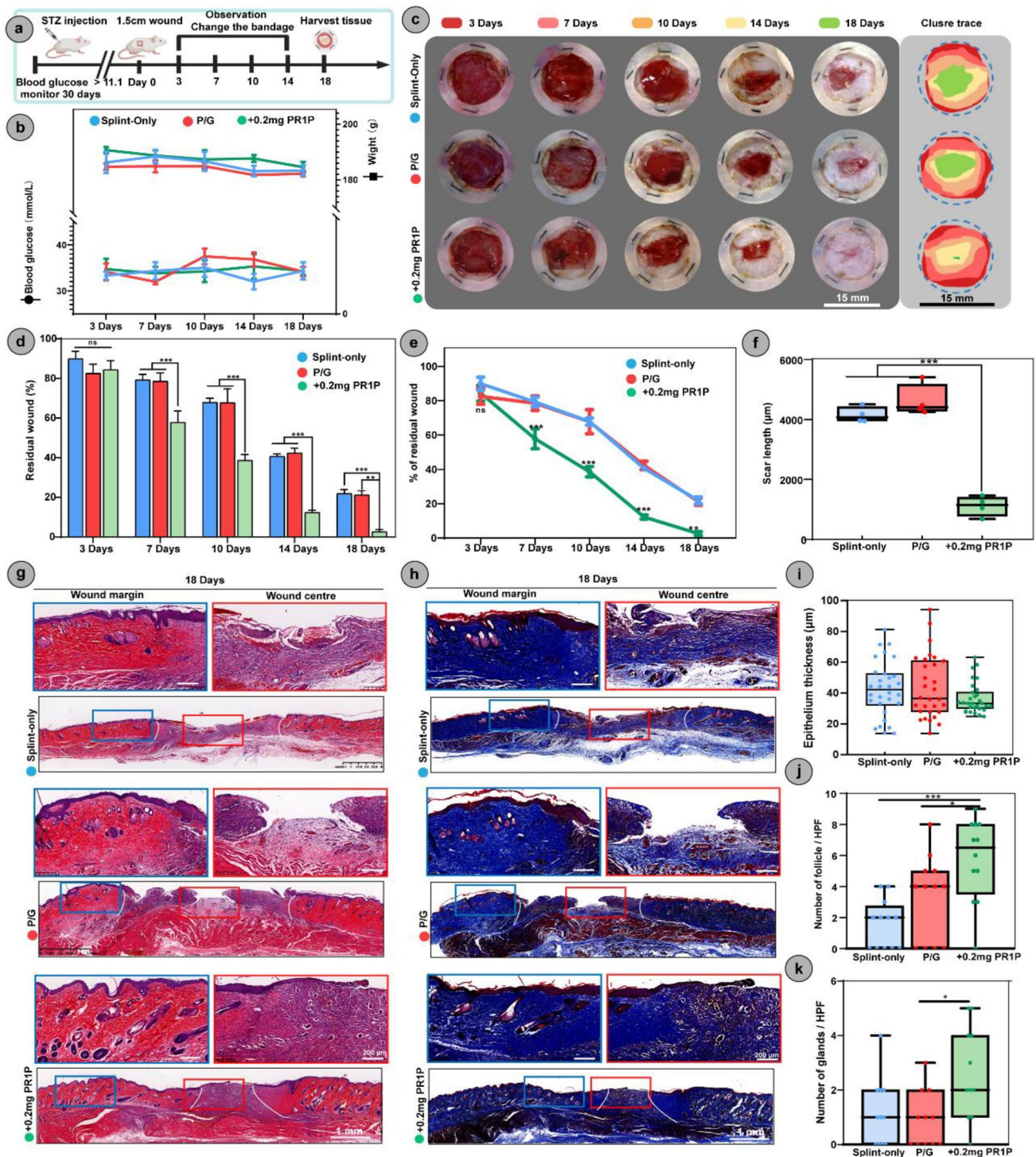
Fig. 10 Validation of the therapeutic effect of the P/G-PR1P bandages in diabetic wounds. **a** Schematic illustration of the process by which a splint-fixed 1.5-cm-diameter excisional wound was generated in Lewis rats with diabetes. **b** Blood glucose curve and weight curve (*n* = 3). **c** Representative images and closure traces of wounds treated with or without a P/G bandage or P/G-PR1P bandage for 18 days. Scale bar, 15 mm. **d** Residual wound area changes within 14 days postwound induction. **e** Wound closure curve. Wound size at each time point was normalized to the wound size on Day 0 (*n* = 3). **f** Quantification of the scar length on Day 18 (*n* = 6). **g–h** Representative image showing H&E staining (**g**) and Masson's trichrome staining (**h**) of full-length skin sections within the area of the splint on Day 18. Scale bar, 1 mm. **i–k** Quantification of diabetic wound functionalization (*n* = 3). Quantification of epithelium thickness (**i**), hair follicle density (**j**), and gland density (**k**). *P < 0.05, **P < 0.01, and ***P < 0.001

its sustained and localized presentation at the injury site, thereby indicating a potentially useful approach to induce rapid wound healing. Thereby, the P/G-PR1P bandage completes its first-loop action in vivo, recruiting a peak of VEGF release, just as in the normal healing process.

In previous studies, the scaffold materials (such as PCL and titanium alloy) were immersed in 0.2 mg/mL PR1P solution to immobilize PR1P to the surface of the scaffold [40, 44, 45], which showed better tissue repair. In this study, we co-spun PR1P into the bandage to afford the sustained release of PR1P. To afford an appropriate concentration of PR1P, we leveraged three different concentrations of PR1P (e.g., 0.002, 0.02, and 0.2 mg/mL). Bandages containing 0.2 mg/mL PR1P afforded wound regeneration within 14 days. At the same time, as a clinical bandage, the price of the bandage needs to be considered, and higher concentrations of PR1P would lead to a several-fold increase in the price of the bandage. Therefore, we finally chose 0.2 mg/mL PR1P for further experiments.

To validate the preclinical therapeutic efficacy of the P/G-PR1P bandages, large-sized splinted excisional wound models were established with both normal and diabetic rats. Since rodent skin is highly elastic and tends to contract rather than reepithelialize to drive wound closure, a splint-fixed excisional wound in rats was able to mimic wound healing through granulation and reepithelialization, similar to the healing mechanisms in human wounds [2, 23, 32]. After injury, VEGF is upregulated at the injury site; however, VEGF levels off as time proceeds. Moreover, as the injury site has many MMP-9 molecules, they can degrade VEGF due to their short half-lives. Therefore, PR1P, if released upon injury, can recruit and stabilize VEGF and maintain its function. Consequently, the sustained and controlled release of PR1P at the injury site may stabilize VEGF, which may in turn promote wound healing by inducing vascularization (Fig. S13).

A three-day period was chosen to change the bandage; because of just the right hydrophobicity, cells do not adhere significantly to the bandage within three days (Fig. S1c), so there is no secondary damage to the wound from the bandage change. However, another reason to transplant fresh bandages on Day 3 was to furnish the continuous release of PR1P. In vitro release kinetics revealed the release of PR1P in the first 3 days (Fig. 1m). Upon exposure to the moist environment of host tissues, the gelatin can be dissolved, which may afford the release of PR1P within 3 days. Thus, timely implantation of new bandages may ensure the sustained release of PR1P at the injury site. However, another reason is based on the common clinical practice in wound healing, which involves the change of the bandage at an interval of three days, which may enable the timely observation of wound healing.

After treatment with the P/G-PR1P bandage, angiogenesis was greatly promoted, and the wound was rapidly filled with scarless neotissue, which was accompanied by rapid reepithelialization and deposition of regular basket weave-like distributed collagen. The development of the neotissue accompanied by the presence and maturity of hair follicles and sweat glands suggested embryonic-like tissue regeneration [24], a phenomenon rarely observed in large rat wounds. Remarkably, regeneration of peripheral nerves was also observed, indicating that the tactile sensation of the new skin was similar to that of normal skin. All the aforementioned biological processes were further validated by RNA-Seq. In summary, our findings revealed that the P/G-PR1P bandage met the major goals for skin regeneration, which involve the rapid restoration of barrier function with reduced scarring while promoting tissue function. Moreover, the same therapeutic effect was observed in the diabetic models, which demonstrated the ability of the P/G-PR1P bandages to treat complex wounds.

Interestingly, in addition to enhanced angiogenesis, polarized M2 macrophages and activated fibroblasts were also observed, thus indicating that PR1P could provide additional benefits to wound regeneration. To better elucidate the exact mechanism of these benefits, RNA-Seq was carried out. The results suggested that the wound microenvironment was regulated by the P/G-PR1P bandage, which was the regulatory effect of PR1P on endothelial cells, macrophages, and fibroblasts.

The regulation of endothelial cells was primarily reflected in angiogenesis and vessel development, which was corroborated both by IF staining and RNA-Seq results. RNA-Seq further indicated that the process of angiogenesis was associated with upregulated VEGF, higher oxidative stress, and increased nitric oxide (NO) production in wounds.

M2 macrophages and fibroblasts are critical mediators of tissue regeneration [46–50]. IF staining revealed the polarization of macrophages towards the M2 phenotype in vitro, which was regulated by PR1P-recruiting bandages. RNA-Seq indicated recruitment of monocytes in vitro, which regulated the higher expression of polarization-related genes, such as mTOR and V-ATPase, which were altered at the transcript level. Similarly, the activation of fibroblasts was observed in vivo, which resulted in the deposition of ECM components, such as collagen.

Interestingly, fibroblasts did not benefit after PR1P-recruiting VEGF treatment in vitro. Meanwhile, in vitro experiments revealed that the P/G-PR1P bandage was indeed effective in recruiting VEGF, regulating endothelial cells, and modulating the polarization of macrophages towards the M2 phenotype. Therefore, the effect of the P/G-PR1P bandage on fibroblasts was hypothesized to not directly result from PR1P- or PR1P-recruited VEGF but was indirectly induced by the higher numbers of M2 macrophages.

This hypothesis was confirmed by the Transwell coculture system in vitro, where PR1P recruited VEGF and promoted macrophage M2 polarization; fibroblasts in the coculture system consequently showed higher expression of α-SMA, thereby inducing the activation of fibroblasts.

Rigorously, this hypothesis was confirmed in vivo. The VEGF and VEGF receptors (VEGFR) were blocked to generate the control groups for in vivo experiments. The VEGF-blocked model demonstrated that the dual-functional effects of the P/G-PR1P bandage were initiated on endogenous VEGF recruitment and VEGF signaling pathway activation. Macrophages underwent M2 polarization in response to PR1P-VEGF, which in turn suppressed the expression of inflammatory factors and MMP-9 and further increased the expression of growth factors, such as VEGF and TGF-β, thereby leveraging a conducive microenvironment for functional tissue repair. Fibroblasts were thus activated, and ECM was deposited, which accelerated wound closure and allowed overall healing to return to a virtuous cycle.

The regeneration of skin appendages and peripheral nerves, to some extent, seems to be a bonus for rapid wound closure. The P/G-0.2 mg PR1P bandage accelerated wound closure and induced hair follicle and peripheral nerve regeneration [24]. The P/G-PR1P bandage also induced higher numbers of new capillary networks, which may ensure the rapid diffusion of oxygen and the fast transport of nutrients, thereby improving the regeneration of hair follicles as well as other skin appendages. The P/G-PR1P bandage also promoted the polarization of macrophages towards the M2 phenotype and increased the expression of VEGF. M2 macrophages have been widely reported to promote hair follicle regeneration via the production of cytokines and chemokines. M2 polarization as well as the formation of a rich vascular network may promote wound metabolism and ensure a conducive microenvironment for wound repair, which may positively influence hair follicle regeneration [51–55].

To ascertain the immunogenicity of the P/G-PR1P bandage, immunohistochemical (IHC) staining of CD4^{+} and CD8^{+} T cells in the wounds was performed. T cells were used due to their significant role in immune rejection. The IHC results did not reveal significant infiltration of T cells, thus excluding the immunogenicity risks of the bandages (Fig. S1 2).

There are also some limitations in this study. While the splinted excisional model mimics the healing process of human skin to a large extent, therapeutic efficacy experiments with the P/G-PR1P bandage should be performed with large animals, such as swine or macaques. In addition, clinical trials should also be conducted. In addition to the experiments and trials mentioned above, good manufacturing practice (GMP) is also a challenge for clinical application. Since the bandage components are simple, such as PLGA, gelatin,

and PR1P, the GMP of bandages may be focused mainly on the standardization of the production process and the quality inspection of each batch of the bandages. Furthermore, in view of the critical role of cytokines, which often interact in multiple biological processes related to tissue regeneration and further regulate the microenvironment, appropriate selection of biomaterials is warranted to further harness the therapeutic potential of these membranes. Nonetheless, nanofibrous P/G-PR1P bandages were successfully fabricated and exhibited proangiogenic and immunomodulatory dual functions. The therapeutic benefits were initiated mainly with PR1P-mediated in situ VEGF recruitment and regulated by the VEGF/macrophage/microenvironment axis.

Conclusions

The off-the-shelf available bandages were constructed capable of enhancing endogenous VEGF gradient. P/G-PR1P bandages promoted multifunctional wound regeneration, including promoting hair neogenesis, neurogenesis, and collagen remodeling. We deciphered that the PR1P-mediated therapeutic effects were mainly governed by pro-angiogenic and immunomodulatory dual-function, which were plausibly based on the VEGF/macrophage/microenvironment axis. Taken together our approach focusing PR1P-mediated in situ recruitment of VEGF may hold great promise for wound healing as other related regenerative medicine and tissue engineering disciplines, including myocardial infarction, limb ischemia, and cerebral ischemia, which largely rely on revascularization following ischemic events.

References

1. Eming SA, Martin P, Tomic-Canic M. Wound repair and regeneration: mechanisms, signaling, and translation. *Sci Transl Med* **2014**;*6*(265):265sr6.

2. Singer AJ, Clark RAF. Cutaneous wound healing. *New Engl J Med* **1999**;*341*:738–46.

3. Sen CK, et al. Human skin wounds: a major and snowballing threat to public health and the economy. *Wound Repair Regen* **2009**;*17*:763–71.

4. Lou D, Luo Y, Pang Q, Tan W, Ma L. Gene-activated dermal equivalents to accelerate healing of diabetic chronic wounds by regulating inflammation and promoting angiogenesis. *Bioact Mater* **2020**;*5*:667–79.

5. Matoori S, Veves A, Mooney DJ. Advanced bandages for diabetic wound healing. *Sci Transl Med* **2021**. https://doi.org/10.1126/scitranslmed.abe4839 .

6. Brown LF, et al. Expression of vascular permeability factor (vascular endothelial growth factor) by epidermal keratinocytes during wound Healing. *J Exp Med* **1992**;*176*:1375–9.

7. Nissen NN, et al. Vascular endothelial growth factor mediates angiogenic activity during the proliferative phase of wound healing. *Am J Pathol* **1998**;*152*:1445–52.

8. Certelli A, et al. Robust angiogenesis and arteriogenesis in the skin of diabetic mice by transient delivery of engineered VEGF and PDGF-BB proteins in fibrin hydrogels. *Front Bioeng Biotechnol* **2021**. https://doi.org/10.3389/fbioe.2021.688467 .

9. Wu J, et al. Mussel-inspired surface immobilization of heparin on magnetic nanoparticles for enhanced wound repair via sustained release of a growth factor and M2 macrophage polarization. *Acs Appl Mater Inter* **2021**;*13*:2230–44.

10. Wang P, et al. In situ formed anti-inflammatory hydrogel loading plasmid DNA encoding VEGF for burn wound healing. *Acta Biomater* **2019**;*100*:191–201.

11. Masters KS. Covalent growth factor immobilization strategies for tissue repair and regeneration. *Macromol Biosci* **2011**;*11*:1149–63.

12. Sheng L, et al. A novel "hot spring"-mimetic hydrogel with excellent angiogenic properties for chronic wound healing. *Biomaterials* **2021**;*264*:120414.

13. Hu S, et al. A mussel-inspired film for adhesion to wet buccal tissue and efficient buccal drug delivery. *Nat Commun* **2021**. https://doi.org/10.1038/s41467-021-21989-5 .

14. Ahn S, et al. Biomimetic and estrogenic fibers promote tissue repair in mice and human skin via estrogen receptor β. *Biomaterials* **2020**;*255*:120149.

15. Srifa W, et al. Cas9-AAV6-engineered human mesenchymal stromal cells improved cutaneous wound healing in diabetic mice. *Nat Commun* **2020**. https://doi.org/10.1038/s41467-020-16065-3 .

16. Flora T, de Torre IG, Alonso M, Rodríguez-Cabello JC. Tethering QK peptide to enhance angiogenesis in elastin-like recombinamer (ELR) hydrogels. *J Mater Sci - Mater Med* **2019**;*30*:30.

17. Zisch AH, Schenk U, Schense JC, Sakiyama-Elbert SE, Hubbell JA. Covalently conjugated VEGF–fibrin matrices for endothelialization. *J Control Release* **2001**;*72*:101–13.

18. Zhao W, McCallum SA, Xiao Z, Zhang F, Linhardt RJ. Binding affinities of vascular endothelial growth factor (VEGF) for heparin-derived oligosaccharides. *Biosci Rep* **2011**;*32*:71–81.

19. Adini A, et al. A novel strategy to enhance angiogenesis in vivo using the small VEGF-binding peptide PR1P. *Angiogenesis* **2017**;*20*:399–408.

20. Yuan Z, et al. Vascular endothelial growth factor-capturing aligned electrospun polycaprolactone/gelatin nanofibers promote patellar ligament regeneration. *Acta Biomater* **2022**;*140*:233–46.

21. Zhang X, et al. Electroactive electrospun nanofibers for tissue engineering. *Nano Today* **2021**;*39*:101196.

22. Chen L, et al. Programmable immune activating electrospun fibers for skin regeneration. *Bioact Mater* **2021**;*6*:3218–30.

23. Abbas Shafiee ASCN, Friedrich AREJ. Convergence of 3D printed biomimetic wound dressings and adult stem cell therapy. *Biomaterials* **2020**;*268*:120558.

24. Griffin DR, et al. Activating an adaptive immune response from a hydrogel scaffold imparts regenerative wound healing. *Nat Mater* **2021**;*20*:560–9.

25. Peng LH, et al. Self-adaptive all-in-one delivery chip for rapid skin nerves regeneration by endogenous mesenchymal stem cells. *Adv Funct Mater* **2020**;*30*:2001751.

26. Shen Y, et al. Sequential release of small extracellular vesicles from bilayered thiolated alginate/polyethylene glycol diacrylate hydrogels for scarless wound healing. *ACS Nano* **2021**;*15*:6352–68.

27. Yuan Z, et al. Vascular endothelial growth factor-capturing aligned electrospun polycaprolactone/gelatin nanofibers promote patellar ligament regeneration. *Acta Biomater* **2021**;*140*:233–46.

28. Monika P, Waiker PV, Chandraprabha MN, Rangarajan A, Murthy KNC. Myofibroblast progeny in wound biology and wound healing studies. *Wound Repair Regen* **2021**;*29*:531–47.

29. Puthia M, et al. A dual-action peptide-containing hydrogel targets wound infection and inflammation. *Sci Transl Med* **2020**. https://doi.org/10.1126/scitranslmed.aax6601 .

30. Ishihara J, et al. Laminin heparin-binding peptides bind to several growth factors and enhance diabetic wound healing. *Nat Commun* **2018**;*9*(1):1–4.

31. Yamakawa S, Hayashida K. Advances in surgical applications of growth factors for wound healing. *Burns Trauma* **2019**. https://doi.org/10.1186/s41038-019-0148-1 .

32. Sorg H, Tilkorn DJ, Hager S, Hauser J, Mirastschijski U. Skin wound healing: an update on the current knowledge and concepts. *Eur Surg Res* **2017**;*58*:81–94.

33. Goonoo N, Bhaw-Luximon A. Mimicking growth factors: role of small molecule scaffold additives in promoting tissue regeneration and repair. *Rsc Adv* **2019**;*9*:18124–46.

34. Xia Y, et al. ZnO/nanocarbons-modified fibrous scaffolds for stem cell-based osteogenic differentiation. *Small* **2020**;*16*:2003010.

35. Xie L, et al. Ti-MOF-based biosafety materials for efficient and long-life disinfection via synergistic photodynamic and photothermal effects. *Biosaf Health* **2022**;*4*:135–46.

36. Li Z, et al. Photothermally tunable biodegradation of implantable triboelectric nanogenerators for tissue repairing. *Nano Energy* **2018**;*54*:390–9.

37. Wang A, et al. Piezoelectric nanofibrous scaffolds as in vivo energy harvesters for modifying fibroblast alignment and proliferation in wound healing. *Nano Energy* **2018**;*43*:63–71.

38. Xia Y, et al. Multivalent polyanionic 2D nanosheets functionalized nanofibrous stem cell-based neural scaffolds. *Adv Funct Mater* **2021**;*31*:2010145.

39. Qian Y, Lin H, Yan Z, Shi J, Fan C. Functional nanomaterials in peripheral nerve regeneration: scaffold design, chemical principles and microenvironmental remodeling. *Mater Today* **2021**;*51*:165–87.

40. Zhao Z, et al. Chimeric peptides quickly modify the surface of personalized 3D printing titanium implants to promote osseointegration. *Acs Appl Mater Inter* **2021**;*13*:33981–94.

41. Luo R, Dai J, Zhang J, Li Z. Accelerated skin wound healing by electrical stimulation. *Adv Healthc Mater* **2021**;*10*:2100557.

42. Zhan L, et al. Grooved fibers: preparation principles through electrospinning and potential applications. *Adv Fiber Mater* **2022**;*4*:203–13.

43. Long Y, et al. Effective wound healing enabled by discrete alternative electric fields from wearable nanogenerators. *ACS Nano* **2018**;*12*:12533–40.

44. Adini A, et al. PR1P stabilizes VEGF and upregulates its signaling to reduce elastase-induced murine emphysema. *Am J Resp Cell Mol* **2020**;*63*:452–63.

45. Schumacher M, Habibović P, van Rijt S. Peptide-modified nano-bioactive glass for targeted immobilization of native VEGF. *Acs Appl Mater Inter* **2022**;*14*:4959–68.

46. Li X, et al. Adventitial fibroblast-derived vascular endothelial growth factor promotes vasa vasorum-associated neointima formation and macrophage recruitment. *Cardiovasc Res* **2020**;*116*:708–20.

47. Witherel CE, Abebayehu D, Barker TH, Spiller KL. Macrophage and fibroblast interactions in biomaterial-mediated fibrosis. *Adv Healthc Mater* **2019**;*8*(4):1801451.

48. Hadrian K, et al. Macrophage-mediated tissue vascularization: similarities and differences between cornea and skin. *Front Immunol* **2021**;*12*:667830.

49. Chu C, et al. Modulation of foreign body reaction and macrophage phenotypes concerning microenvironment. *J Biomed Mater Res A* **2019**;*108*:127–35.

50. Chen Y, et al. Interactions between immunomodulatory biomaterials and immune microenvironment: cues for immunomodulation strategies in tissue repair. *Front Bioeng Biotechnol* **2022**. https://doi.org/10.3389/fbioe.2022.820940 .

51. Wise LM, Stuart GS, Real NC, Fleming SB, Mercer AA. VEGF receptor-2 activation mediated by VEGF-E limits scar tissue formation following cutaneous injury. *Adv Wound Care* **2018**;*7*:283–97.

52. Abaci HE, et al. Tissue engineering of human hair follicles using a biomimetic developmental approach. *Nat Commun* **2018**;*9*(1):1–11.

53. Kim D, et al. Noncoding dsRNA induces retinoic acid synthesis to stimulate hair follicle regeneration via TLR3. *Nat Commun* **2019**;*10*(1):1–3.

54. Wang X, et al. Macrophages induce AKT/β-catenin-dependent Lgr5+ stem cell activation and hair follicle regeneration through TNF. *Nat Commun* **2017**;*8*(1):1–4.

55. Li M, et al. CCL5 deficiency promotes liver repair by improving inflammation resolution and liver regeneration through M2 macrophage polarization. *Cell Mol Immunol* **2020**;*17*:753–64.

Authors and Affiliations

Yi Chen[1,2] · Zhengchao Yuan[3] · Weiyan Sun[1,2] · Shafiq Muhammad[3,6,8] · Jun Zhu[4] · Jiafei Chen[1,2] · Hai Tang[1,2] · Ling Hu[5] · Weikang Lin[1,2] · Yanxi Zeng[7] · Long Wang[1,2] · Lei Zhang[1,2] · Yunlang She[1,2] · Hui Zheng[1,2] · Guofang Zhao[9,10] · Dong Xie[1,2] · Xiumei Mo[3] · Chang Chen[1,2]

1. Department of Thoracic Surgery, Shanghai Pulmonary Hospital, Tongji University, Shanghai 200092, China

2. Shanghai Engineering Research Center of Lung Transplantation, Shanghai 200433, China

3. State Key Laboratory for Modification of Chemical Fibers and Polymer Materials, Shanghai Engineering Research Center of Nano-Biomaterials and Regenerative Medicine, College of Biological Science and Medical Engineering, Donghua University, Shanghai 201620, China

4. Center for Life Science, Tsinghua University, Beijing 100084, China

5. State Key Laboratory of Medical Neurobiology and MOE Frontiers Center for Brain Science, Institutes of Brain Science, Fudan University, Shanghai 200433, China

6. Department of Chemical Engineering, Faculty of Engineering, Graduate School, Kyushu University, Fukuoka 819-0395, Japan

7. Department of Cardiology, Shanghai Tenth People's Hospital, School of Medicine, Tongji University, Shanghai 200092, China

8. Department of Biotechnology, Faculty of Science and Technology, University of Central Punjab (UCP), Lahore 54000, Pakistan

9. Department of Cardiothoracic Surgery, Hwa Mei Hospital, University of Chinese Academy of Sciences, Ningbo 315000, China

10. Ningbo Institute of Life and Health Industry, University of Chinese Academy of Sciences, Ningbo 315000, China